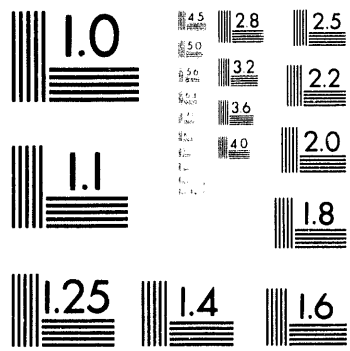
1.0
1.1
1.25
1.4
1.6
1.8
2.0
2.2
2.5
2.8
3.2
3.6
4.0
4.5
5.0
5.6

1 of 1

SAND91-2850 • TTC-1251
Unlimited Release
Printed September 1993

Distribution
Category UC-722

A Constitutive Model for Layered Wire Mesh and Aramid Cloth Fabric

M. K. Neilsen
Engineering Mechanics and Material Modeling Department
Sandia National Laboratories, Albuquerque, NM 87185

J. D. Pierce
Transportation Systems Department
Sandia National Laboratories, Albuquerque, NM 87185

R. D. Krieg
Engineering Science and Mechanics
University of Tennessee, Knoxville, TN 37996

Abstract

A new package for the air transport of hazardous materials is currently being developed in the Transportation Systems Department at Sandia National Laboratories. The baseline design has a unique impact limiter which uses layers of aluminum screen wire and aramid cloth fabric. A primary motivation for selecting this unusual combination of materials is the need for the impact limiter to not only limit the amount of load transmitted to the primary container but also remain in place during impact events so that it provides a thermal barrier during a subsequent fire. A series of uniaxial and confined compression tests indicated that the layered material does not behave like other well characterized materials. No existing constitutive models were able to satisfactorily capture the behavior of the layered material; thus, a new plasticity model was developed. The new material model was then used to characterize the response of air transport packages with layered impact limiters to hypothetical accidental impact events. Responses predicted by these analyses compared favorably with experiments at Sandia's rocket sled test facility in which a one-fourth scale package was subjected to side and end impacts at velocities of 428 and 650 fps, respectively.

Acknowledgements

The experimental impact tests which are documented in this report were performed at Sandia's rocket sled test facility by William Kampfe and the Rocket and Dynamics Test Team. The dedication and hard work by Dennis Bolton to procure hardware, fabricate test articles, and coordinate the instrumentation and testing is especially appreciated. Thanks also to Duane Stenberg for his efficient assistance in instrumenting the test articles. The assistance provided by the finite element code sponsors, Mike Stone and Steve Attaway, during the implementation of the new material model is gratefully acknowledged.

Contents

Tables

Figures

1. Introduction

A new package for the air transport of hazardous materials is currently being developed in the Transportation Systems Department at Sandia National Laboratories. The baseline design has a unique impact limiter which uses multiple layers of aluminum screen wire and Kevlar 49[1] cloth fabric. A primary motivation for selecting this unusual combination of materials is the need for the impact limiter to not only limit the amount of load transmitted to the primary, internal container but also remain in place throughout impact events so that it provides a thermal barrier during a possible subsequent fire. If the thermal insulation provided by the aluminum screen wire and the Kevlar fabric is not sufficient, then layers of insulating materials such as ceramic cloth may be added to the composite stack-up.

The mechanical behavior of the layered material was partially characterized by a series of uniaxial and confined compression tests. These tests indicated that in compression the strength and stiffness of the material is nearly isotropic; however, in tension the material is quite anisotropic. In a direction normal to the layers, the material has no tensile strength; whereas, in a direction parallel to the layers the material has a significant amount of tensile strength.

A constitutive model for the layered wire mesh and Kevlar fabric was needed to numerically investigate the behavior of air transport packages during accidental impact events. A review of existing constitutive models indicated that a plasticity model which was recently developed for rigid polyurethane foams by Neilsen, Morgan, and Krieg [1] could be modified to capture the isotropic crush behavior of the layered wire mesh and Kevlar fabric material. Results from the uniaxial and confined compression tests were used to obtain material parameters for the new layered material model. The uniaxial and confined compression tests were then analyzed to ensure that the model captured the material behavior exhibited during these tests.

The new isotropic layered material model accurately simulated the material responses exhibited during the material characterization tests; however, as expected, this isotropic plasticity model was not able to capture the anisotropic behavior of the layered material in tension. The effects of this weakness on impact limiter behavior predictions were evaluated by comparing results from analyses which used the new layered material model with analyses in which layers of wire mesh and Kevlar fabric were actually modeled using a technique developed by Attaway [2]. This evaluation indicated that reasonable predictions of impact limiter behavior during a typical impact event could be obtained with the new isotropic plasticity model.

---

[1] E.I. duPont de Nemours & Co., Inc.

Next, a steel container with a composite layered wire mesh and Kevlar fabric impact limiter was subjected to a 424 feet per second side impact. This impact event was analyzed to further benchmark the new layered material model. Finally, a 428 fps side impact test and a 650 fps end impact test were recently performed on scale model packages with composite layered material impact limiters. Finite element analyses of these hypothetical accident events are compared with experimental observations in this report. Results from both the finite element analyses and the experiments indicate that the layered wire mesh with Kevlar fabric material will remain intact even during a 650 fps impact event if an adequate number of Kevlar layers are used. However, the layered wire mesh with Kevlar fabric limiter allows for the transmission of high loads to the primary inner container. The primary container was not plastically deformed during the 424 fps side impact event but was plastically deformed during the 650 fps end impact event. The amount of load transmitted to the primary container can be reduced by introducing layers of material which absorb more energy than the wire mesh into the impact limiter stack-up. The analyses presented in this report also reveal that the behavior of the contents (material inside the primary container) can have a significant positive or negative effect on primary container deformation. Content behavior must be considered in the development of air transport package designs.

2. Experimental Data

The behavior of layers of aluminum wire mesh with and without Kevlar fabric was characterized with a series of uniaxial compression and confined compression tests. In the uniaxial compression tests, the samples were compressed in one direction and allowed to expand in directions which are orthogonal to the loading direction. In the confined compression tests, the samples were compressed in one direction and not allowed to expand in the directions orthogonal to the loading direction. All of the samples used in the confined compression tests were manufactured by alternatively stacking up 20 layers of aluminum wire mesh and 2 layers of Kevlar fabric. The wire mesh has an initial wire diameter of 0.0105 inches, and the Kevlar fabric has a thickness of 0.017 inches. The undeformed samples had a cubical shape with an edge dimension of 2.0 inches. The samples were loaded at various angles relative to the layer stack-up direction. Axial stress versus axial engineering strain curves generated during the confined compression tests are shown in Figures 2.1 and 2.2. In these figures, a positive axial stress or strain is compressive. These tests indicate that layer orientation has little effect on the response of the material; thus, the response of the material to compressive loads is nearly isotropic. Also, the compressive strength, σ^c, varies exponentially with axial engineering strain, ϵ, as shown in Figure 2.2. The solid line in Figures 2.1 and 2.2 represents a best fit to the experimental confined compression test data which is given by the following equation

$$\sigma^c = 17.0\epsilon^{8.68\epsilon} \tag{2.1}$$

Since the lateral displacements are constrained, the axial engineering strain, ϵ, has the same magnitude as the engineering volume strain, ϵ_{vol}, in these tests.

In a second set of tests, layers of wire mesh and wire mesh with Kevlar fabric were unconfined and subjected to cyclic uniaxial loads (Figure 2.3). The applied load was oriented normal to the wire mesh and fabric layers (i.e. a layer orientation of 0 degrees was used). The number of Kevlar layers and the sample size was allowed to change. Various sample sizes were used to determine if the lateral constraint due to friction at the load platen to sample interface had any effect on the axial response of the layered material. In the first test, a sample with a length of 6.0 inches, a width of 7.0 inches and the height of 1.0 inch was used. In the remaining three tests, samples with lengths and widths of 2.0 inches and heights of 1.0 inch were used. In the first two uniaxial compression tests, the layering was identical to the layering used in the confined compression tests: 3 X (20 Aluminum wire mesh / 2 Kevlar fabric) for a total of 60 aluminum wire mesh layers and 6 Kevlar fabric layers. In the last two experiments, the Kevlar layers were eliminated and a total of 62 layers of aluminum wire mesh were used. These tests indicate that inclusion of the Kevlar fabric layers will slightly reduce the axial strain magnitude at which the

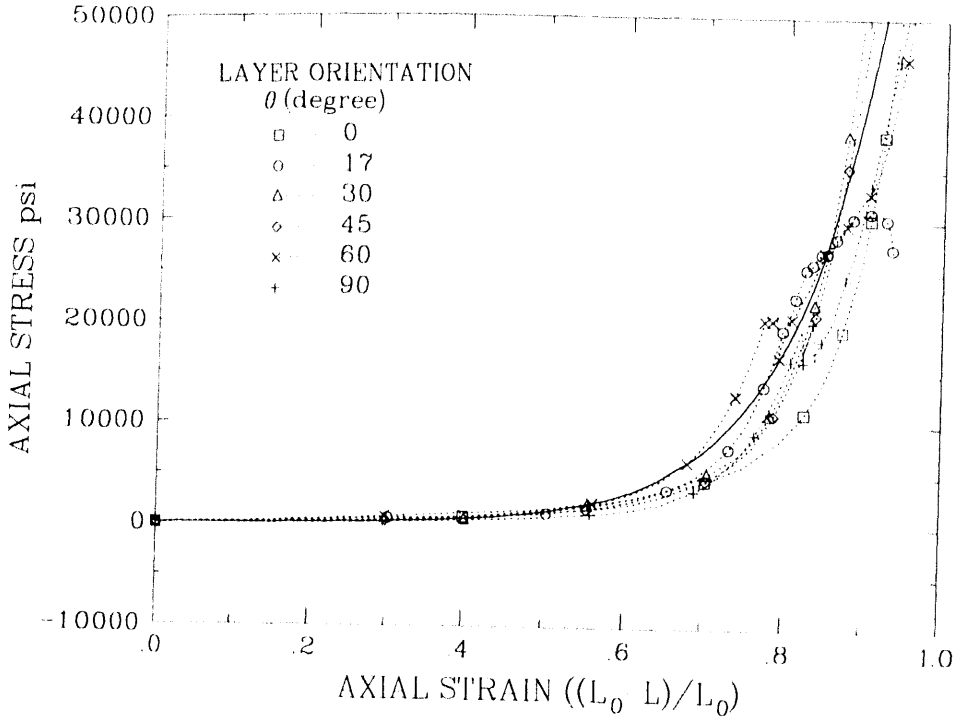

Figure 2.1. Results from Confined Compression Tests.

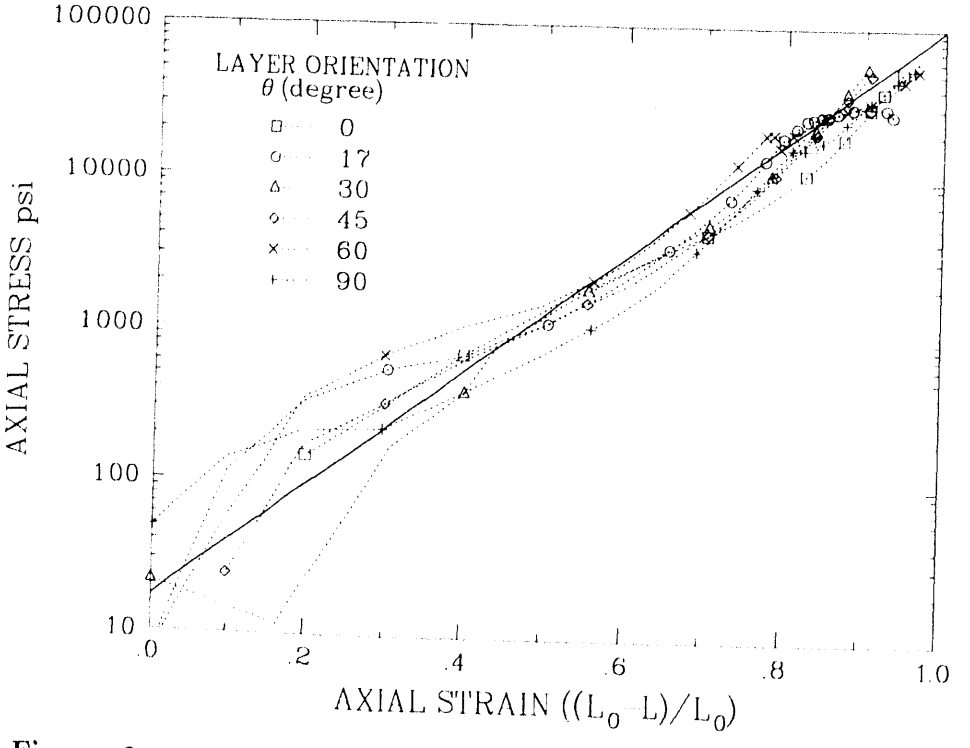

Figure 2.2. Results from Confined Compression Tests on a Linear-Log Plot.

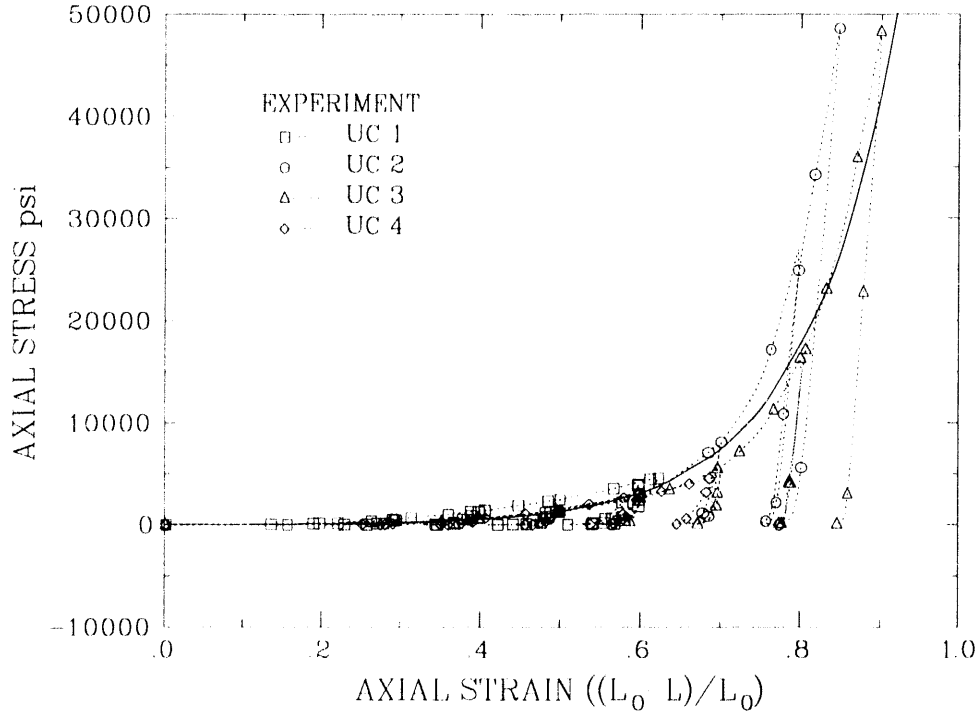

Figure 2.3. Results from Uniaxial Compression Tests.

load carrying capacity of the layered material begins to significantly increase. This occurs because the Kevlar fabric is much stiffer than the wire mesh in compression. Also, these experiments indicate that the lateral strains generated by uniaxial compression are small. Measurements of the deformed samples after the unconfined compression tests indicated that the lateral deformation generated during Tests UC 1 and UC 4 was negligible and during Tests UC 2 and UC 3 the sample width permanently increased from 2.0 inches to 2.2 inches. This means that the material has a Poisson's ratio that is nearly equal to zero. Furthermore, any plasticity model that is developed to capture the behavior of this material should predict small lateral strains when the material is loaded into the plastic regime. The solid line in Figure 2.3 represents a best fit to the confined compression test data (Equation 2.1). Results from the limited number of uniaxial compression tests indicates that Equation 2.1 also represents the uniaxial compression data reasonably well. Since the layered material exhibited small lateral strains during the unconfined, uniaxial compression tests, the confining stress generated during the zero degree confined compression tests must have been small. Thus, the zero degree confined compression tests and the unconfined compression tests subjected the layered material to nearly the same load path and the material behavior during these tests was nearly identical.

In tension, the layered material exhibits widely varying behavior. For example, when a single layer of wire mesh is loaded in-plane, it has a tensile strength of approximately 75 lbs per inch of width [3]. A single Kevlar fabric layer has an in-plane tensile strength of 1400 lbs per inch of width [3]. The aluminum wire mesh has a much smaller in-plane strain to failure than the Kevlar fabric; thus, the in-plane tensile strength of the layered

material is equal to the maximum of the in-plane tensile strength of the Kevlar fabric or the aluminum wire mesh alone. When the layered material is loaded in a direction normal to the fabric layers the material exhibits essentially no strength as the layers are separated.

3. Review of Existing Plasticity Models

A variety of finite element codes, SANTOS [4], PRONTO-2D [5] and PRONTO-3D [6], have been developed at Sandia National Laboratories to efficiently solve large solid mechanics problems on the CRAY-YMP. In this chapter, a number of plasticity theories which have been implemented in these codes are reviewed. The capability of these theories to capture layered material behavior are then evaluated by simulating the material characterization tests with the quasi-static code SANTOS [4]. Once appropriate material models and parameters for the layered material are identified, impact events can be simulated using the transient dynamic analysis codes PRONTO-2D [5], and PRONTO-3D [6].

Plasticity theories are characterized by their yield function, Ψ, and their evolution equation for plastic deformation. The yield function defines a surface in stress space which bounds stress states for which the response of the material is elastic. The flow rule defines the nature of plastic deformation. In the finite element codes listed above, the material models are expressed in terms of the unrotated Cauchy stress, $\boldsymbol{\sigma}$, and the deformation rate, $\mathbf{d}$, in the unrotated configuration [6]. The deformation rate or stretching tensor is additively decomposed into its elastic, $\mathbf{d}^{el}$, and plastic, $\mathbf{d}^{pl}$, parts as follows:

$$\mathbf{d} = \mathbf{d}^{el} + \mathbf{d}^{pl} \tag{3.1}$$

The plastic part of the stretching tensor is given by the flow rule

$$\mathbf{d}^{pl} = \dot{\omega}\mathbf{g} \tag{3.2}$$

where $\dot{\omega}$ defines the magnitude of the plastic strain increment and the second-order tensor $\mathbf{g}$ defines the orientation of the plastic strain increment. The constitutive relation is given by

$$\dot{\boldsymbol{\sigma}} = \mathbf{E} : \mathbf{d}^{el} \tag{3.3}$$

where $\mathbf{E}$ is the fourth-order elasticity tensor and the double dot indicates a contraction on two of the indices. Thus in indicial notation, Equation 3.3 would be written as follows:

$$\dot{\sigma}_{ij} = E_{ijkl}\, d^{el}_{kl} \tag{3.4}$$

Equations 3.1 to 3.3 can by combined to obtain the following expression:

$$\dot{\boldsymbol{\sigma}} = \mathbf{E} : (\mathbf{d} - \dot{\omega}\mathbf{g}) \tag{3.5}$$

All of the constitutive theories reviewed in this chapter assume that the elastic response is linear and isotropic; thus, $\mathbf{E}$ is given by

$$\mathbf{E} = 3K\mathbf{P}^{sp} + 2G\mathbf{P}^{d} \tag{3.6}$$

where K is the bulk modulus and G is the shear modulus. The bulk and shear moduli are related to Young's modulus, E, and Poisson's ratio, ν, as follows

$$K = \frac{E}{3(1-2\nu)} \qquad G = \frac{E}{2(1+\nu)} \tag{3.7}$$

The fourth-order spherical projection operator, $\mathbf{P}^{sp}$, and the deviatoric projection operator, $\mathbf{P}^{d}$, are given by

$$\mathbf{P}^{sp} = \frac{1}{3}\mathbf{i} \otimes \mathbf{i} \qquad \mathbf{P}^{d} = \mathbf{I} - \mathbf{P}^{sp} \tag{3.8}$$

where $\mathbf{I}$ is the symmetric fourth-order identity tensor, and $\mathbf{i}$ is the second-order identity. In indicial notation, the symmetric fourth-order identity and the projection operators can be expressed as follows:

$$I_{ijkl} = \frac{1}{2}(\delta_{ik}\delta_{jl} + \delta_{il}\delta_{jk}) \qquad P^{sp}_{ijkl} = \frac{1}{3}\delta_{ij}\delta_{kl} \qquad P^{d}_{ijkl} = I_{ijkl} - P^{sp}_{ijkl} \tag{3.9}$$

where δ_{ij} is the Kronecker delta.

In the remainder of this chapter, three different plasticity models which are currently available in finite element codes are reviewed to determine if any of them can capture the behavior exhibited by the layered material. The three models include a von Mises or conventional deviatoric plasticity model, a soil and crushable foam model which was developed by Krieg [7], and a rigid polyurethane foam model [1].

3.1 Von Mises

The von Mises or conventional deviatoric plasticity model is available in most solid mechanics finite element codes. It has a yield function given by

$$\Psi = \sigma - k \qquad \sigma = (\tfrac{3}{2}\boldsymbol{\sigma}^{d} : \boldsymbol{\sigma}^{d})^{\frac{1}{2}} \tag{3.10}$$

where σ is the von Mises effective stress, k is the deviatoric yield strength, and $\boldsymbol{\sigma}^{d}$ is the deviatoric stress tensor. The associated flow rule for this model is as follows:

$$\mathbf{d}^{pl} = \dot{\omega}\frac{\boldsymbol{\sigma}^{d}}{(\boldsymbol{\sigma}^{d} : \boldsymbol{\sigma}^{d})^{\frac{1}{2}}} \tag{3.11}$$

The yield function, $\Psi = 0$, mathematically represents a yield surface that is an infinitely long cylinder with the hydrostat as its axis. The flow rule for this model indicates that the plastic deformations are purely deviatoric and that the volume of the material does not permanently change. This model is obviously not appropriate for the layered material which exhibits significant permanent volume changes when it is crushed.

3.2 Soil and Crushable Foam

The soil and crushable foam model [7] uses two separate yield functions, one for the volumetric response and one for the deviatoric response. This model assumes that the volumetric response is independent of the deviatoric response but that the deviatoric response depends on the mean stress. The yield functions and flow rule for this model are as follows:

$$\Psi^{sp} = p - f(e_{vol}) \tag{3.12}$$

$$\Psi^{d} = \sigma - (a_0 + a_1 p + a_2 p^2) \tag{3.13}$$

$$\mathbf{d}^{pl} = \dot{\omega}^{sp}\mathbf{i} + \dot{\omega}^{d}\mathbf{g}^{d} \qquad \mathbf{g}^{d} = \frac{\boldsymbol{\sigma}^{d}}{(\boldsymbol{\sigma}^{d} : \boldsymbol{\sigma}^{d})^{\frac{1}{2}}} \tag{3.14}$$

where e_{vol} is the engineering volume strain, p is the mean stress, $p = -\boldsymbol{\sigma} : \mathbf{i}/3$, and $\mathbf{i}$ is the second-order identity. The deviatoric yield function, $\Psi^{d} = 0$, represents a surface which depends on the mean stress, and the volumetric yield function, $\Psi^{sp} = 0$, represents a planar cap normal to the hydrostat. The evolution equation for plastic deformation indicates that both volumetric and deviatoric permanent deformations can be generated with this model. Since f in Equation 3.12 can be chosen to accurately describe the volumetric response of the layered material, this material model should be able to capture the layered material behavior exhibited during the confined compression tests.

3.3 Rigid Polyurethane Foam

The rigid polyurethane foam model [1] has yield functions and a flow rule given by

$$\Psi^{i} = \boldsymbol{\sigma} : \mathbf{P}^{i} : \boldsymbol{\sigma} - h(e_{vol}) \qquad i = 1,2,3 \tag{3.15}$$

$$\mathbf{d}^{pl} = \dot{\omega}^{1}\mathbf{P}^{1} : \boldsymbol{\sigma} + \dot{\omega}^{2}\mathbf{P}^{2} : \boldsymbol{\sigma} + \dot{\omega}^{3}\mathbf{P}^{3} : \boldsymbol{\sigma} \tag{3.16}$$

$\mathbf{P}^{i}$ is the fourth-order principal projection operator defined as follows:

$$\mathbf{P}^{i} = \mathbf{n}^{i} \otimes \mathbf{n}^{i} \otimes \mathbf{n}^{i} \otimes \mathbf{n}^{i} \qquad i = 1,2,3 \tag{3.17}$$

where $\mathbf{n}^{i}$ is a vector oriented in a principal stress direction. The yield functions, $\Psi^{i} = 0$, actually represent 3 pairs of planar yield surfaces with normals given by $\mathbf{n}^{i}$. The flow rule for this model indicates that a permanent deformation increment may be associated with each principal stress direction depending on the magnitude of the principal stress. This model can capture the behavior exhibited by the layered material in the uniaxial

and confined compression tests if an appropriate form for the function h in Equation 3.15 is selected. Also, this model can be modified to exhibit behavior in tension which is significantly different than its behavior in compression by simply making the function h in Equation 3.15 depend on the sign of the principal stress.

4. Development of a New Layered Material Model

In this chapter, a new layered material model which is similar in many respects to the existing rigid polyurethane foam model [1] is developed. This new model, like the existing rigid foam model, has yield functions expressed in terms of principal stresses. The static uniaxial and confined compression tests indicated that an appropriate form for the compressive yield function would be as follows

$$\Psi^i = -\sigma^i - ae^{-be_{vol}} \tag{4.1}$$

where σ^i is a principal stress which is negative in compression, a and b are material constants and e_{vol} is the engineering volume strain which is also negative in compression. In tension, we assume that the material is elastic perfectly plastic. Thus, the yield function for tensile principal stresses is

$$\Psi^i = \sigma^i - \tau \tag{4.2}$$

where τ is a material constant that represents the isotropic tensile strength of the layered material. These yield functions represent three pairs of intersecting planar yield surfaces. The flow rule for the new layered material model is identical to the flow rule for the rigid polyurethane foam model, Equation 3.16.

The new layered material model was implemented in the static and dynamic finite elements codes SANTOS [4], PRONTO-2D [5], and PRONTO-3D [6]. The sponsors of these codes have made the material subroutines and interfaces nearly identical; thus, implementation of the model into several codes was nearly as easy as implementation into a single code. In these codes, the new material is referred to as WIRE MESH and uses the material cues given in Table 4.1.

Table 4.1. Material Cues for the New Layered Material Model

Cue	Units	Description
YOUNGS MODULUS	Force/Length^2	
POISSONS RATIO		
A	Force/Length^2	a in Eq. 4.1
B		b in Eq. 4.1
TENSION	Force/Length^2	τ in Eq. 4.2

5. Simulation of Material Characterization Tests

In this chapter, we attempt to use both the soil and crushable foam model and the new layered material model to simulate the layered material behavior exhibited during the uniaxial compression tests which were presented in Chapter 2.

5.1 Soil and Crushable Foam Model

With the soil and crushable foam model [7], the user is required to prescribe the volumetric response of the material. Since no hydrostatic compression tests were performed on the layered material, results from the confined compression tests were used to estimate the hydrostatic response of the layered material. In the confined compression tests, the engineering volume strain is equal to the measured axial strain because lateral displacements were constrained during these tests. Unfortunately, the confining stress was not measured during the confined compression tests. The mean stress generated during these tests was estimated by assuming that the confining stress was negligible compared with the axial stress and that the mean stress is, thus, approximately equal to the axial stress divided by 3. The user is also required to prescribe the dependence of the deviatoric yield surface on the mean stress by defining the material parameters a_0, a_1, and a_2 in Equation 3.11. Since there was not enough experimental data to characterize this dependence, three analyses were completed using various combinations of material parameters a_0, a_1, and a_2. The primary purpose of these analyses was to determine if material parameters a_0, a_1, and a_2 could be selected such that the material behavior exhibited during the unconfined compression tests by the layered material could be captured with this material model.

These analyses were performed using a one element model of an axisymmetric material specimen (Figure 5.1) and the quasistatic finite element code SANTOS [4]. The model was subjected to a uniaxial compressive load to simulate the experimental, unconfined compression tests. Material parameters given in Table 5.1 were used in these analyses.

Table 5.1. Material Parameters for the Soil and Crushable Foam Model

Analysis Number	Elastic Modulus (psi)	Poisson's Ratio	a_0 (psi)	a_1	a_2 (1/psi)
5.1	1.0×10^5	0.0	100.0	0.0	0.0
5.2	1.0×10^5	0.0	100.0×10^6	0.0	0.0
5.3, 5.4	1.0×10^5	0.0	0.1	3.0	0.0

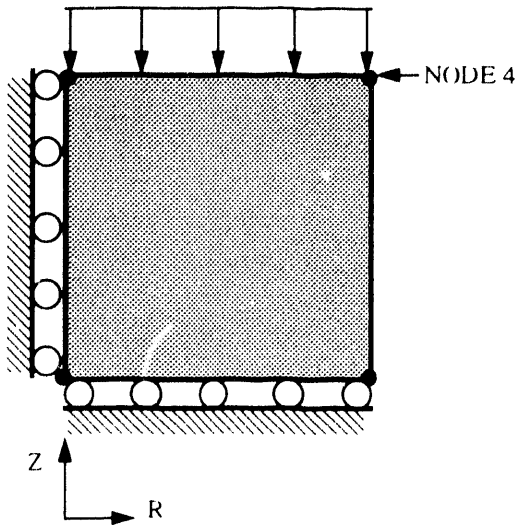

Figure 5.1. Axisymmetric Finite Element Model of Material Specimen

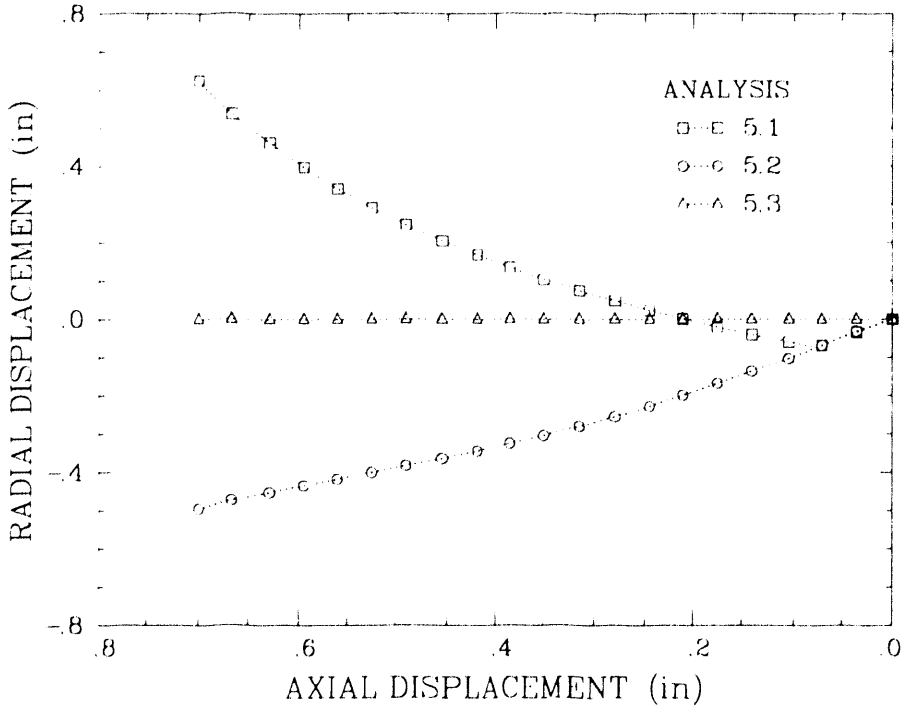

Figure 5.2. Axial and Radial Displacement of Node 4 During the Simulation of the Unconfined Compression Test - Soil and Crushable Foam Material Model

In Analysis 5.1, the material was given a low deviatoric yield strength of 100 psi. When the sample was compressed in the axial direction, it exhibited large displacements in the radial direction (Figure 5.2). This significant radial expansion of a material specimen subjected to unconfined compression is typical for soils but was certainly not exhibited by the layered wire mesh, Kevlar fabric material when it was compressed in a direction normal to the layers.

In Analysis 5.2, the layered material was given a large deviatoric yield strength of 10.0×10^6 psi. With this high deviatoric yield strength, the model exhibited radial contraction when it was compressed in the axial direction (Figure 5.2). This occurs because the selection of a large deviatoric yield strength prevents the generation of any deviatoric plastic strains and only allows for the generation of volumetric plastic strains. This radial contraction associated with uniaxial compression is not exhibited by the layered material.

In Analysis 5.3, the material parameters were chosen such that the deviatoric yield surface and the uniaxial load path are nearly coincident (Figure 5.3). The deviatoric yield surface and uniaxial load path would be identically coincident if a value of 0.0 psi was used for material parameter a_0; however, a_0 is required to be positive so that the material has at least some tensile strength. Thus, a small positive value of 0.1 psi was used for a_0. This choice of material parameters is expected to allow for the generation of both volumetric and deviatoric plastic strains when the material is subjected to uniaxial compression. With these material parameters, the finite element analysis of the uniaxial compression test predicted only small radial displacements when the sample was compressed in the axial direction (Figure 5.2). This analysis indicates that by using the third set of deviatoric yield function parameters, $a_0 = 0.1$, $a_1 = 3.0$, and $a_2 = 0.0$, this model will predict the behavior exhibited by the layered material subject to uniaxial compression in a direction normal to the layers.

Next, the cyclic unconfined compression test on the layered material was analyzed using the soil and crushable foam model and the third set of deviatoric yield function parameters. A comparison of analytical and experimental results (Figure 5.4) indicates that the soil and crushable foam model does capture the compressive behavior of the layered material. In Figure 5.4, a positive axial stress or strain is compressive. In tension, the layered material exhibits either a significant amount of tensile strength or layer separation depending on the orientation of the tensile loads. The soil and crushable foam model is not able to capture the significant reduction in material stiffness associated with layer separation and instead predicts plastic deformation at very low tensile stress levels. Unfortunately, no plasticity model will be able to capture the material behavior associated with layer separation, and a much more complex, coupled plasticity-continuum damage theory is needed if capturing this tensile behavior is important.

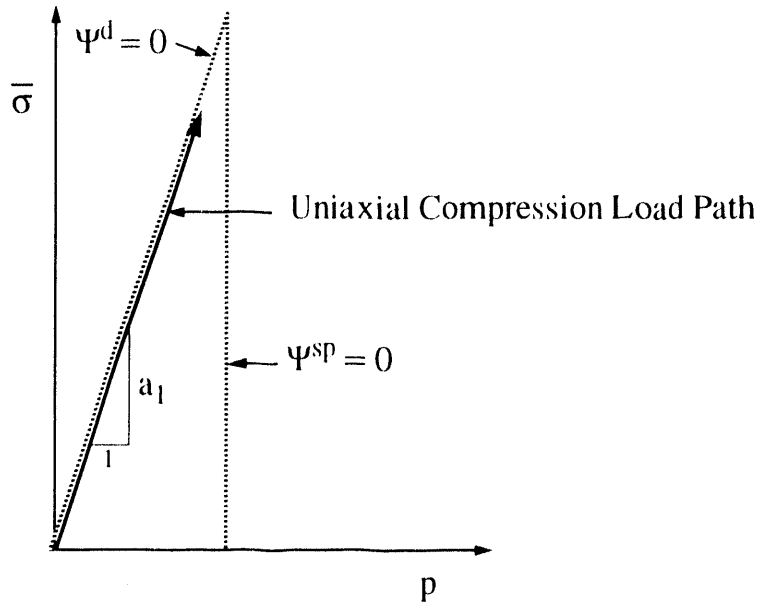

Figure 5.3. Uniaxial Compression Load Path and Yield Surfaces in Mean Stress-Effective Stress Plane.

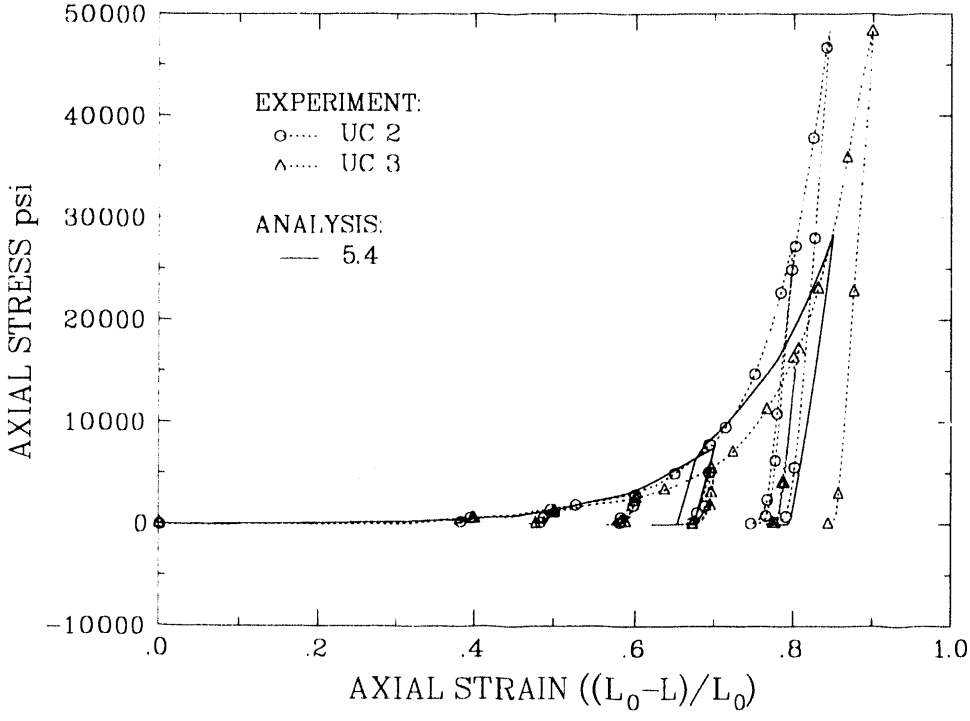

Figure 5.4. Comparison of Analysis 5.4 with Experiment - Uniaxial Compression (Positive Axial Stress is Compressive).

5.2 New Layered Material Model

In this section, the uniaxial compression tests are analyzed using the new layered material model to determine if this model captures the behavior exhibited by the layered material. The one element model of an axisymmetric material specimen shown in Figure 5.1 was used in these analyses. The model was subjected to a cyclic, uniaxial, compressive load to simulate a uniaxial compression test. Material parameters given in Table 5.2 were used in these analyses.

Table 5.2. Material Parameters for the New Layered Material Model

Analysis Number	Elastic Modulus (psi)	Poisson's Ratio	a (psi)	b	τ (psi)
5.5	1.0×10^5	0.0	17.0	8.68	20.0
5.6	1.0×10^5	0.0	17.0	8.68	12.0×10^3
5.7	1.0×10^5	0.0	120.0	8.68	12.0×10^3

In Analysis 5.5, material parameters which are appropriate for loading in a direction perpendicular to the layers, as in the unconfined compression test, were used. When the finite element model was compressed in the axial direction, it accurately predicted a layered material behavior of axial deformation only. In Analysis 5.6, the material was given a large tensile strength which is appropriate for loading in a direction parallel to the layers. Again, the model accurately represented the axial compression of the material (Figure 5.5), and in tension the material exhibited a significant amount of tensile strength. This response is appropriate for layered material loaded in a direction parallel to the layers. In Analysis 5.7, material parameter a was increased to 120.0 psi. This analysis indicated that the axial strain associated with densification and a significant increase in the load carrying capacity of the layered material can be modified by changing material parameter a (Figure 5.5). If the layered material is precompressed during manufacture of the impact limiter, then material parameter a can be modified to account for this precompression. These analyses indicate that with an appropriate selection of material parameters, uniaxial compression tests on the layered material can be simulated with the new layered material model. This new model can be given either very little or a significant amount of tensile strength without changing the compressive response of the model. This feature was attractive for the layered material, since it exhibits tensile behavior which is significantly different than its compressive behavior.

Unfortunately, no plasticity model will be able to capture the significant reduction in material stiffness associated with layer separation or the increase in material stiffness that is generated when the layered material is compressed into the lock-up regime. To capture both changes in the elastic response and the permanent deformations, a much more complex coupled plasticity-continuum damage model will be needed. However, use of the new plasticity model developed in Chapter 4 is expected to generate reasonable

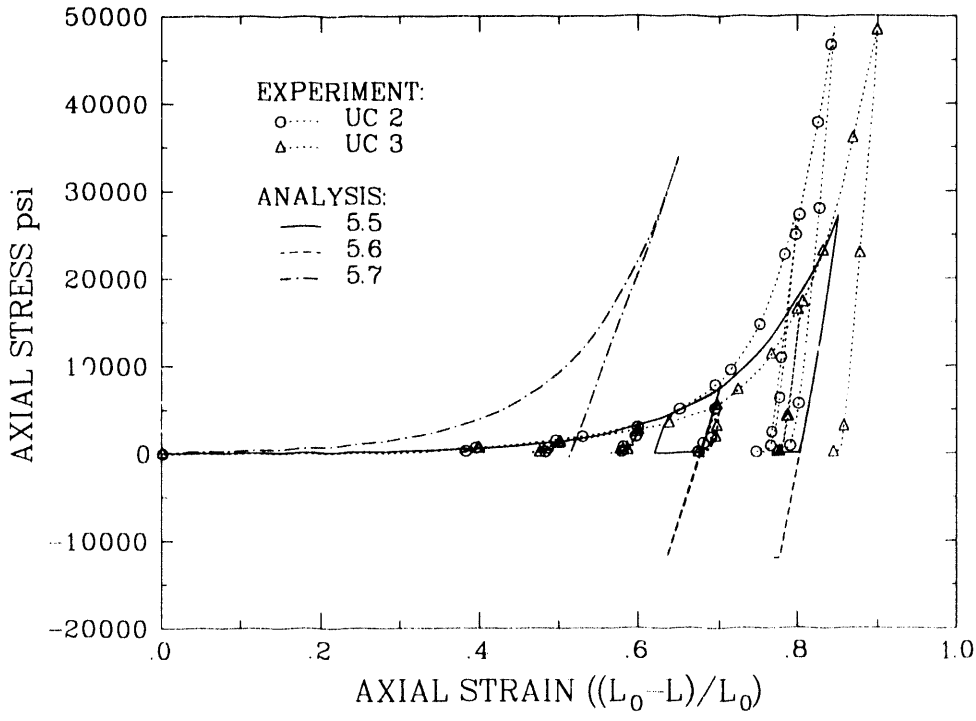

Figure 5.5. Comparison of Analyses 5.5 to 5.7 with Experiments - Uniaxial Compression (Positive Axial Stress is Compressive).

predictions for the behavior of the layered material in an impact limiter during a typical accident event because the amount cyclic loading generated during such an event is negligible. Also, the most important behavior, the permanent deformation and energy absorption of the layered material between the container and the impacting surface, will be captured with the new layered material model.

6. Effect of Layered Material Modeling Variations

In this chapter, a series of two-dimensional, plane strain analyses were performed to investigate the importance of capturing the anisotropic tensile behavior of the layered material during a typical side impact event. These analyses were performed using the finite element model shown in Figure 6.1 and PRONTO-2D [5]. The package impacted a flat, rigid target with an impact velocity of 424 fps in all of these analyses. However, a variety of material models and parameters were used to describe the impact limiter material (Table 6.1). The steel container and contents were modeled as a solid elastic rod with the same weight per unit length as a typical filled container.

In Analysis 6.1, the impact limiter material was simulated using the new layered material model with an isotropic tensile strength of 12,000 psi which is appropriate for loading in a direction parallel to the layers. In Analysis 6.2, the impact limiter was modeled with layers of material with alternating high and low isotropic tensile strength values of 12,000 psi and 20 psi. The dark layers in Figure 6.1 were given a high tensile strength, and the lighter layers were given a low tensile strength. The introduction of low tensile strength layers allows layer separation in a direction normal to the fabric layers. This approach for capturing the orthotropic material behavior with an isotropic constitutive model was developed by Attaway [2] to model the behavior of wood impact limiters. In Analysis 6.3,

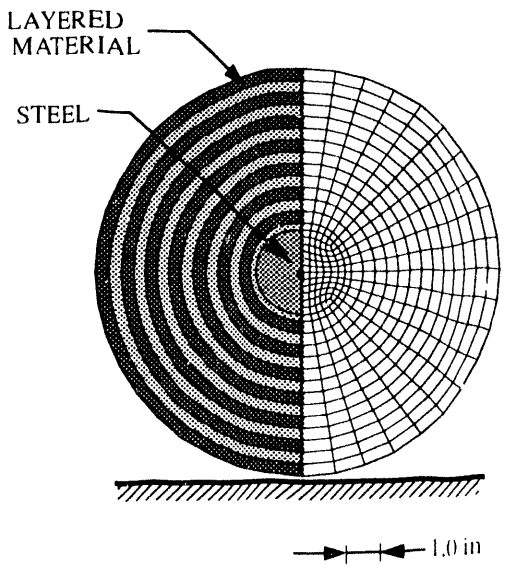

Figure 6.1. Two-Dimensional Plane Strain Model of Package Cross-Section.

Table 6.1. Material Parameters Used in the Evaluation of Layered Material Modeling Variations

Layered Material: New Model						
Analysis Number	Elastic Modulus (psi)	Poisson's Ratio	a (psi)	b	τ (psi)	Density (lb s^2 $in.^{-4}$)
6.1	1.0×10^5	0.0	17.0	8.68	12,000	4.17×10^{-5}
6.2	1.0×10^5	0.0	17.0	8.68	12,000 / 20.0	4.17×10^{-5}
6.3	1.0×10^5	0.0	17.0	8.68	20.0	4.17×10^{-5}
6.4	1.0×10^5	0.0	120.0	8.68	12,000	4.17×10^{-5}

Layered Material: Soil and Crushable Foam Model						
Analysis Number	Elastic Modulus (psi)	Poisson's Ratio	a_0 (psi)	a_1	a_2 (1/psi)	Density (lb s^2 $in.^{-4}$)
6.5	1.0×10^5	0.0	0.1	3.0	0.0	4.17×10^{-5}

Container/Contents: Elastic						
Analysis Number	Elastic Modulus (psi)	Poisson's Ratio	Density (lb s^2 $in.^{-4}$)			
6.1 to 6.5	30.0×10^6	0.3	4.135×10^{-4}			

all of the layers were given a low tensile strength of 20 psi. Results from these analyses indicate that the predicted displacement of the container is rather insensitive to these layer modeling variations (Figure 6.2). Also, nearly identical acceleration-time histories were obtained when all of the layers were given a high tensile strength (Analysis 6.1) and when alternating layers with high and low tensile strength were used (Analysis 6.2). However, the predicted peak acceleration of the container is significantly lower when all of the layers are given a low tensile strength of 20 psi (Figure 6.3).

Plots of the deformed shape of the impact limiter generated during and after the impact event are shown in Figures 6.4 to 6.6. Densification of the layered material between the container and the impacting surface is followed by compression of the layered material above the container. A comparison of the deformed shapes predicted by the first three analyses indicates that the manner in which the layers are modeled affects the predicted deformed shape of the impact limiter. Specifically, inclusion of layers with low tensile strengths tends to increase the predicted amount of lateral deformation generated during the numerical simulation.

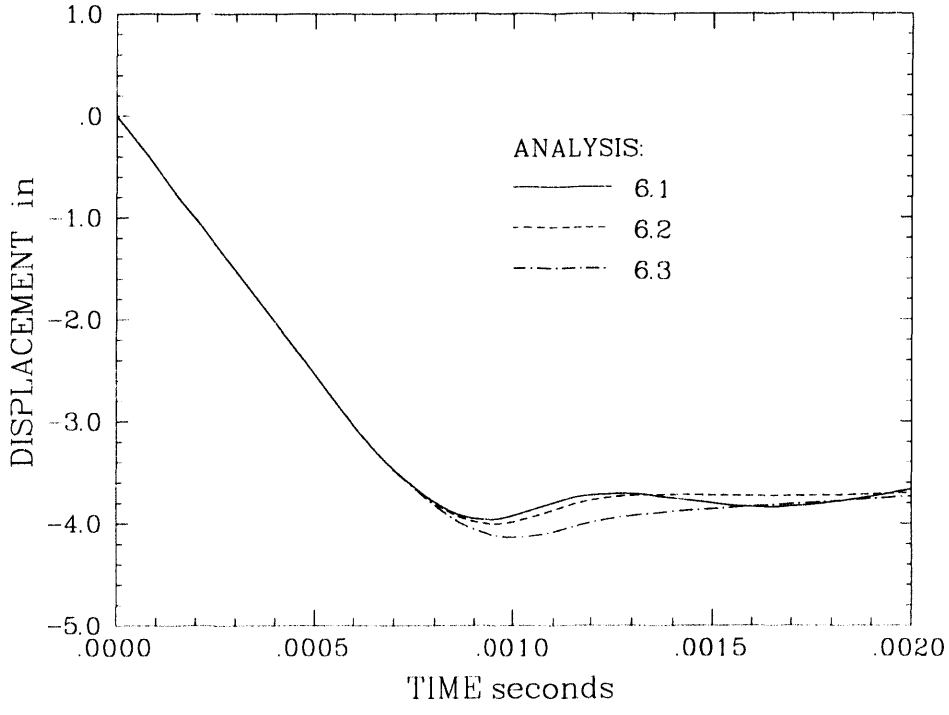

Figure 6.2. Container Displacement Predicted by Analyses with the New Layered Material Model - Effect of Layer Modeling Variations.

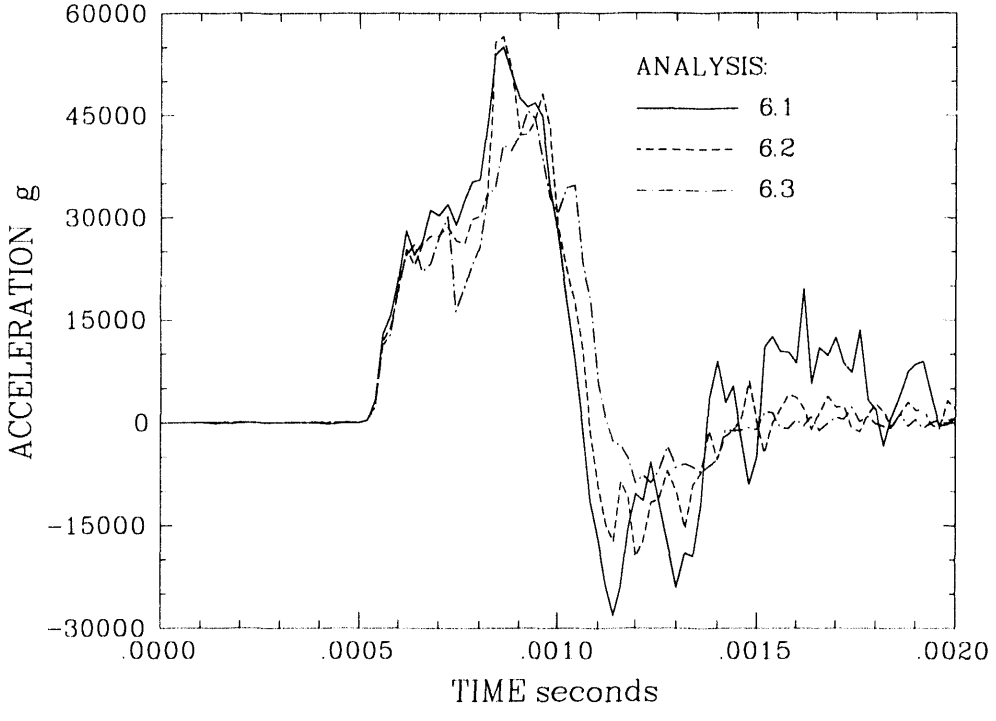

Figure 6.3. Container Acceleration Predicted by Analyses with the New Layered Material Model - Effect of Layer Modeling Variations.

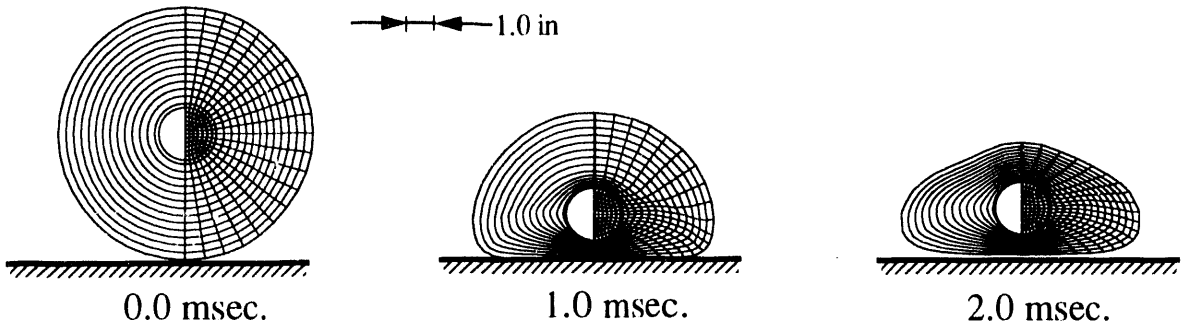

Figure 6.4. Deformed Shape of Finite Element Model at Various Time Steps During Analysis 6.1 - High Isotropic Tensile Strength.

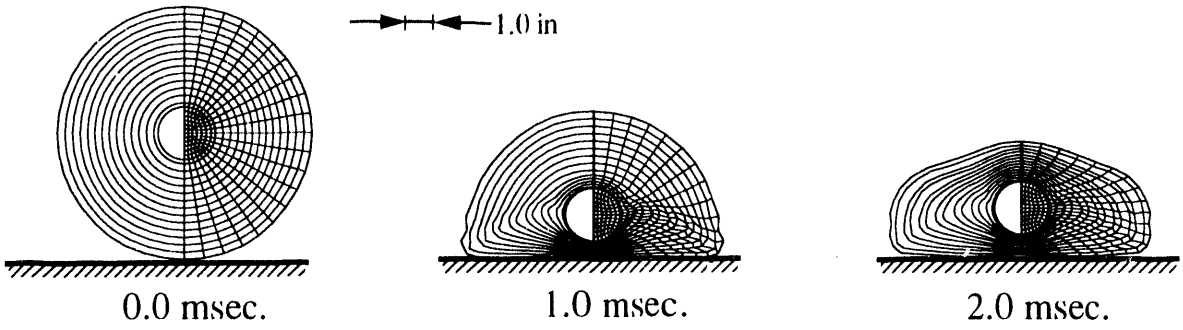

Figure 6.5. Deformed Shape of Finite Element Model at Various Time Steps During Analysis 6.2 - Alternating High/Low Isotropic Tensile Strength.

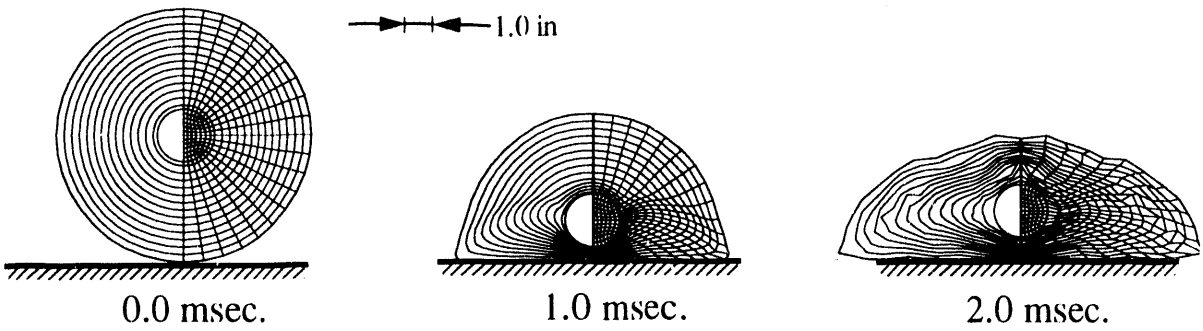

Figure 6.6. Deformed Shape of Finite Element Model at Various Time Steps During Analysis 6.3 - Low Isotropic Tensile Strength.

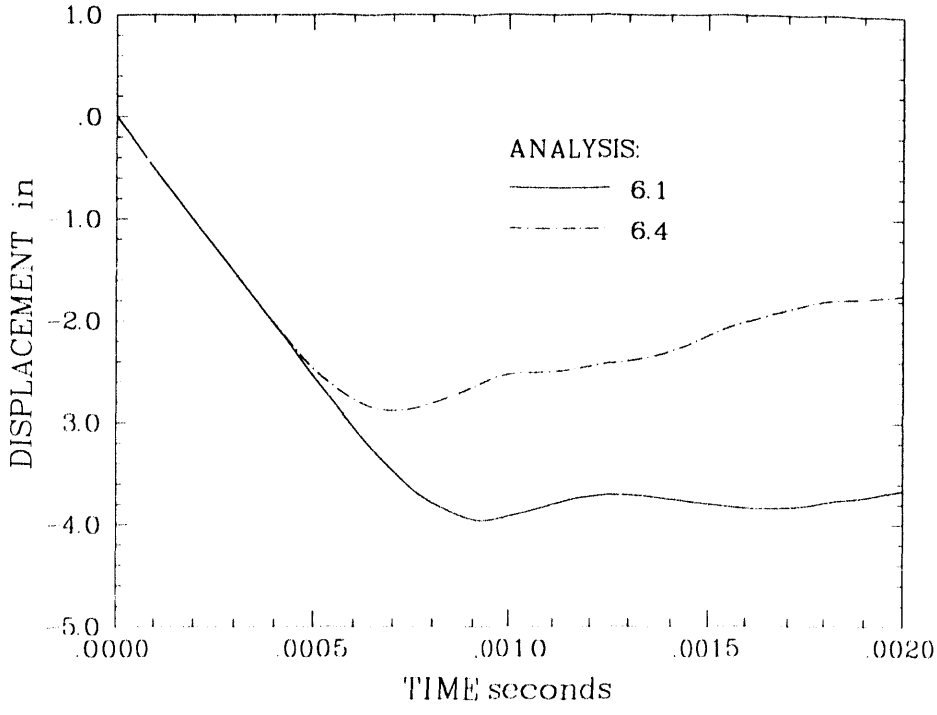

Figure 6.7. Container Displacement Predicted by Analyses with the New Layered Material Model - Effect of Material Parameter a.

In Analysis 6.4, the effects of precompressing the impact limiter during manufacture were investigated by increasing material parameter a to 120 psi. As expected, the predicted amount of impact limiter crush-up is reduced when the limiter material is precompressed and material parameter a is increased (Figure 6.7). However, the predicted peak acceleration of the container is only 10 percent higher when material parameter a is changed from 17 psi to 120 psi (Figure 6.8). Thus, precompression of the layered limiter material during manufacture will have a significant effect on limiter deformation during an impact event but little effect on the loads applied to the primary container. A plot of the deformed shape of the model (Figure 6.9) also shows that an increase in material parameter a reduces the amount of impact limiter deformation.

In Analysis 6.5, the layered material was simulated using the soil and crushable foam model. The material parameters were chosen such that the behavior of the layered material exhibited during the static uniaxial compression tests were captured (Table 6.1). Results obtained with the new layered material model and the soil and crushable foam model are compared in Figures 6.10 and 6.11. Similar container displacement predictions are generated with these two material models. However, when the soil and crushable foam model was used, the solution algorithm became unstable during the later stages of the analysis and failed to generate an acceptable solution (Figure 6.12). The lack of stable behavior can probably be attributed to the low tensile strength needed by the soil and

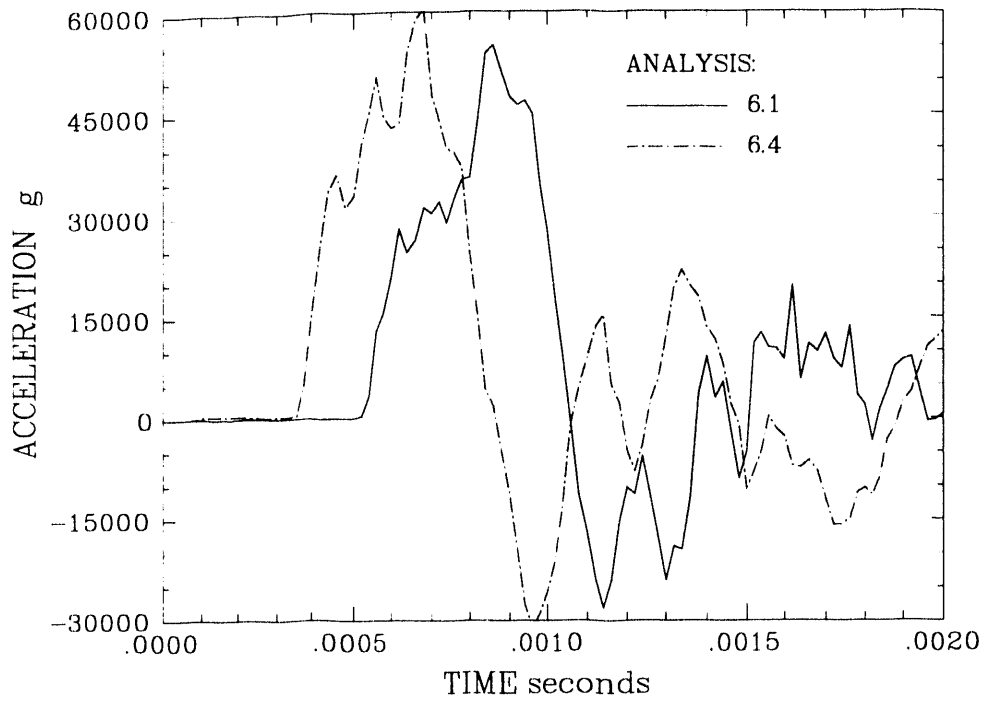

Figure 6.8. Container Acceleration Predicted by Analyses with the New Layered Material Model - Effect of Material Parameter a.

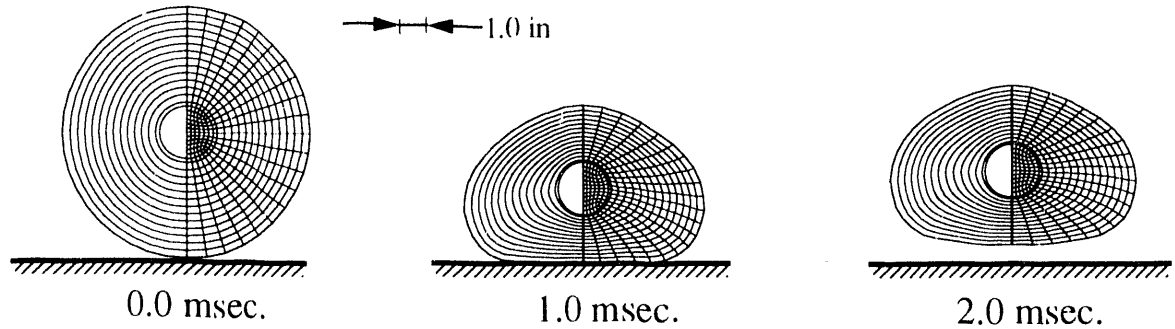

Figure 6.9. Deformed Shape of Finite Element Model at Various Time Steps During Analysis 6.4 - New Layered Material Model with $a = 120$.

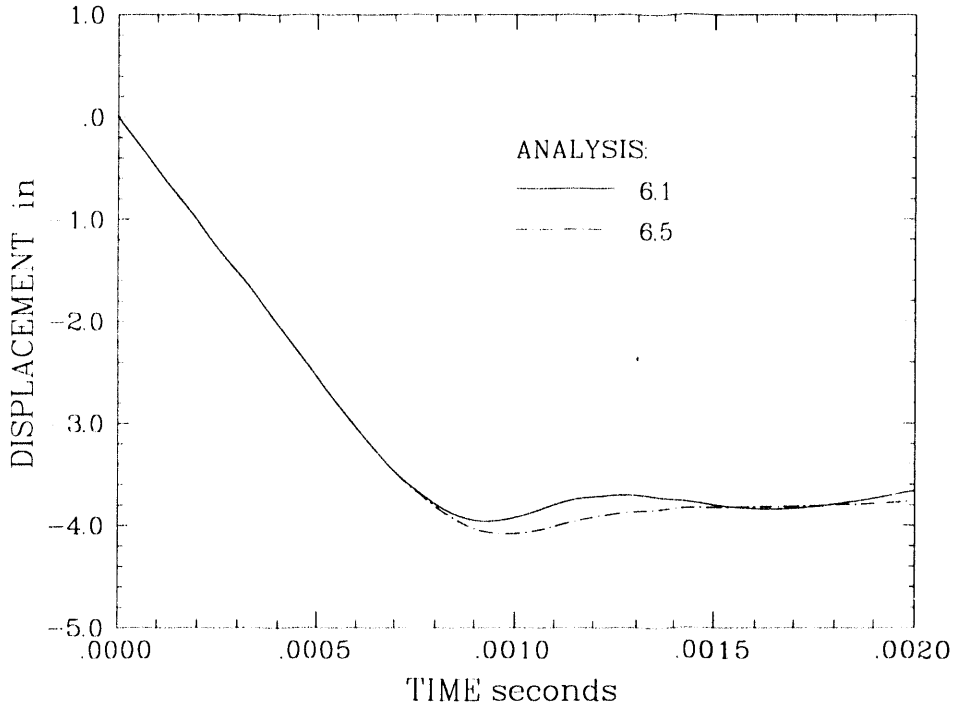

Figure 6.10. Container Displacement Predicted by Analysis 6.5 with the Soil and Crushable Foam Model.

crushable foam model to duplicate the uniaxial compression tests. Since the soil and crushable foam model failed to generate an acceptable solution to this relatively simple two-dimensional problem, it was not used in subsequent three-dimensional analyses.

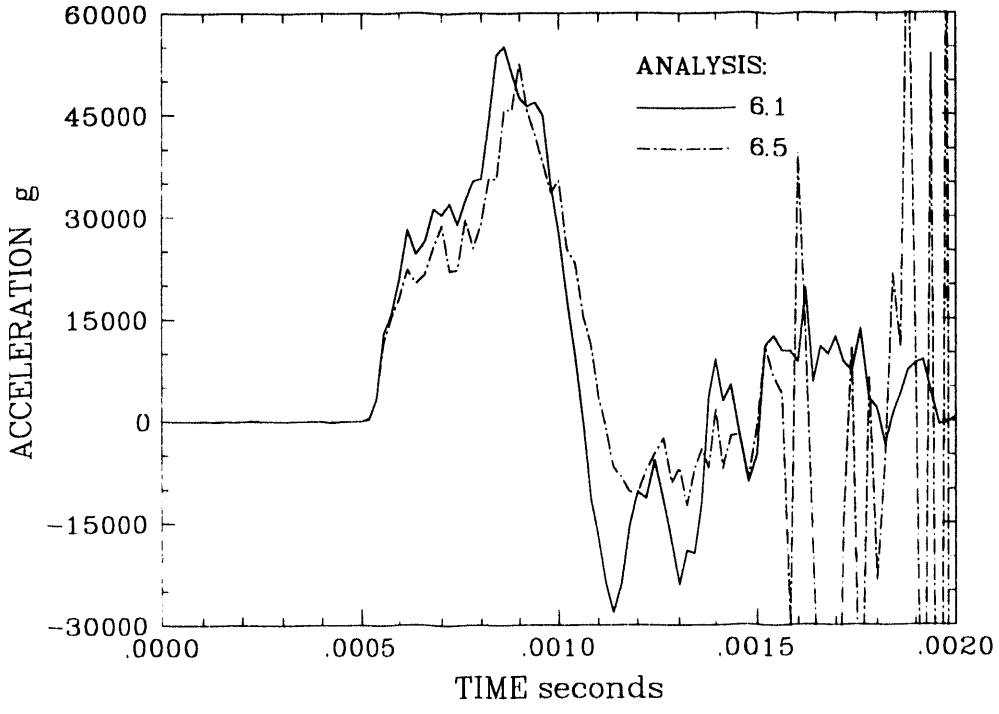

Figure 6.11. Container Acceleration Predicted by Analysis 6.5 with the Soil and Crushable Foam Model.

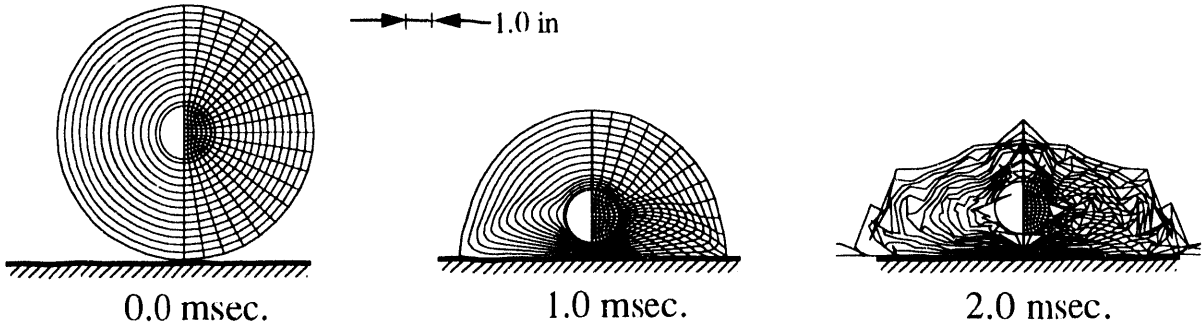

Figure 6.12. Deformed Shape of Finite Element Model at Various Time Steps During Analysis 6.5 - Soil and Crushable Foam Model.

7. Benchmark Analyses - Steel Container with Layered Material Limiter

A package with a steel container and a layered material impact limiter was subjected to a side impact into an essentially unyielding surface with an impact velocity of 424 fps. The purposes of this experiment were to evaluate the behavior of a layered material impact limiter and to generate data to benchmark constitutive models for the layered material. In this chapter, the side impact experiment is analyzed to determine if the new layered material model adequately simulates the impact limiter behavior during this impact event. These analyses were performed using the finite element model shown in Figure 7.1 and PRONTO-3D [6]. Only one-fourth of the package was modeled due to the symmetries present in the package and appropriate boundary conditions were applied to the symmetry planes. The finite element model includes the layered material impact limiter, a steel container, and lead shot contents. Three analyses were performed using various material parameters for the layered material and the lead shot contents (Table 7.1).

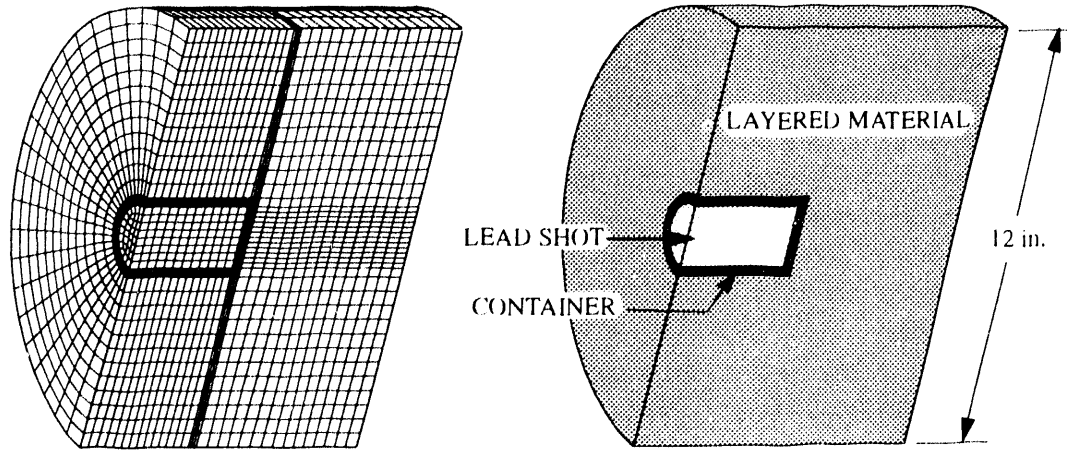

Figure 7.1. Three-Dimensional Finite Element Model of the Benchmark Package with a Steel Container.

In Analysis 7.1, parameters for the layered material were chosen to match the results from the uniaxial material characterization tests. During the manufacture of the package, layers of impact limiter material are wound together and not simply stacked up as they were for the uniaxial compression tests. The winding process generates a compressive stress between the layers and the layers are precompressed prior to the impact event. The amount of precompression will depend on the winding tension and radial location in the winding [8]. Layers near the container will be precompressed significantly more than

Table 7.1. Material Parameters Used in the Benchmark Analyses

Layered Material: New Model						
Analysis Number	Elastic Modulus (psi)	Poisson's Ratio	a (psi)	b	τ (psi)	Density (lb s^2 in^{-4})
7.1	1.0×10^5	0.0	17.0	8.68	12,000	4.17×10^{-5}
7.2, 7.3	1.0×10^5	0.0	120.0	8.68	12,000	4.17×10^{-5}

AS19 Steel Container: Elastic-Plastic						
Analysis Number	Elastic Modulus (psi)	Poisson's Ratio	Yield Strength (psi)	Hardening Modulus (psi)	Beta	Density (lb s^2 in^{-4})
7.1 to 7.3	30.0×10^6	0.3	56.0×10^3	1.5×10^6	0.0	7.72×10^{-4}

Lead Shot: Elastic or Elastic-Plastic						
Analysis Number	Elastic Modulus (psi)	Poisson's Ratio	Yield Strength (psi)	Hardening Modulus (psi)	Beta	Density (lb s^2 in^{-4})
7.1, 7.2	40.0×10^3	0.3	-	-	0.0	3.084×10^{-4}
7.3	2.0×10^6	0.3	1200.0	100.0	0.0	3.084×10^{-4}

layers near the outer surface of the limiter. The effect of a uniform precompression of the layers was investigated by increasing material parameter a to 120.0 psi in Analyses 7.2 and 7.3. In Analyses 7.1 and 7.2, the lead shot was modeled as an elastic material and in Analysis 7.3, the lead shot was modeled as an elastic-plastic material. Material parameters which are appropriate for solid lead were used in Analysis 7.3 [9,10].

Displacement and acceleration histories for the container predicted by these analyses are shown in Figures 7.2 and 7.3. The displacement plots indicate that the amount of layered material deformation generated during an impact event is significantly affected by the amount of precompression generated during assembly (Figure 7.2). The acceleration plots indicate that the container is subjected to a peak acceleration of approximately 60,000 g's. The acceleration plots are not very smooth since plot data was only stored at time intervals of 0.05 msec. due to memory constraints. However, the two-dimensional, plane strain analyses of a section near the center of the container which were presented in the previous chapter also predicted a peak acceleration level of approximately 60,000 g's (Figure 6.8). A PLOT HISTORY option which allows for the storage of the acceleration data at every solution step but only at a limited number of nodes in the finite element mesh was recently implemented in PRONTO-3D [6]. This option can be used in future analyses to generate accurate acceleration history plots.

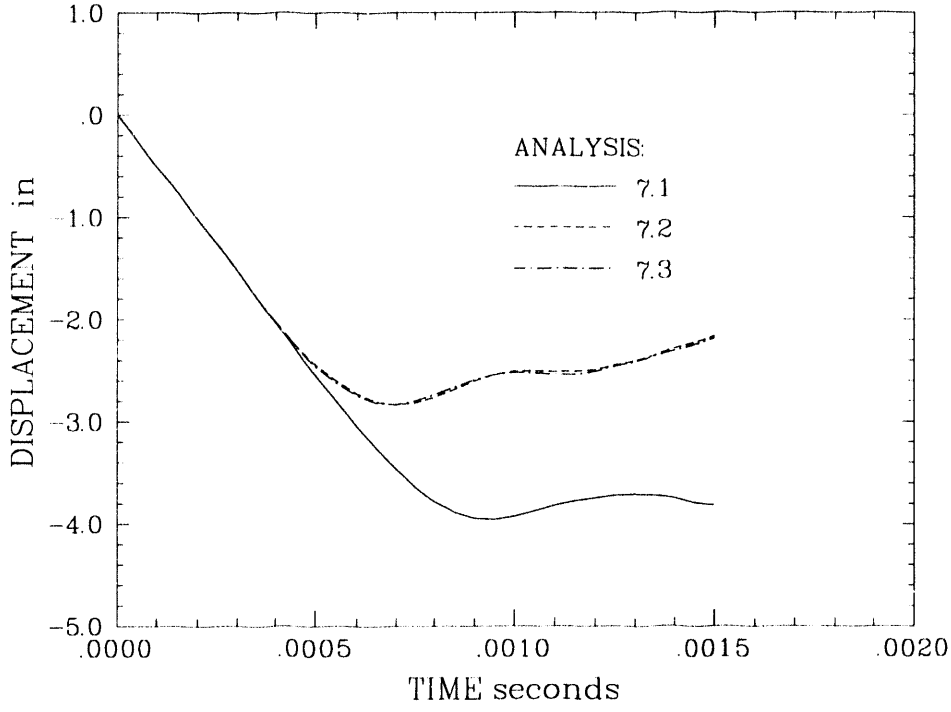

Figure 7.2. Steel Container Displacement Predicted by the Three-Dimensional Finite Element Analyses of a Side Impact.

The cylindrical part of the limiter for this package contained 30 layers of Kevlar fabric and 208 layers of aluminum screen wire. The Kevlar fabric layers alone will give the limiter material an initial tensile strength of 8615 psi in a circumferential direction. As the layered material is crushed, the spacing between the Kevlar layers will decrease and the tensile strength of the layered material will increase if the Kevlar layers are not damaged. The tensile load in a single Kevlar layer was estimated by first computing the principal Cauchy stresses in the layered material between the container and the impact surface. As expected, the maximum tensile stresses were oriented in a direction perpendicular to the package velocity. Element tractions were then computed using the maximum tensile stress and the current element size. Finally, Kevlar layer loads were estimated by dividing the element tractions by the number of Kevlar layers in the element. Recall that the Kevlar layers have a tensile strength of 1400 lbs per inch of width. In Analyses 7.1, 7.2 and 7.3, the predicted maximum Kevlar layer loads are 360, 590, and 560 lbs./inch, respectively. Thus, the Kevlar layers are not expected to fail.

As predicted by these analyses, the layered material limiter did remain in place during the 424 fps side impact test. Unfortunately, during the impact test on the experimental package, lead wires to the accelerometers and strain gages were lost and no experimental gage data was obtained. Therefore, the only comparisons between analysis and experiment which could be made were of the final deformed shape of the package. Deformed shapes of the models predicted during the three analyses are shown in Figures 7.4 to 7.6.

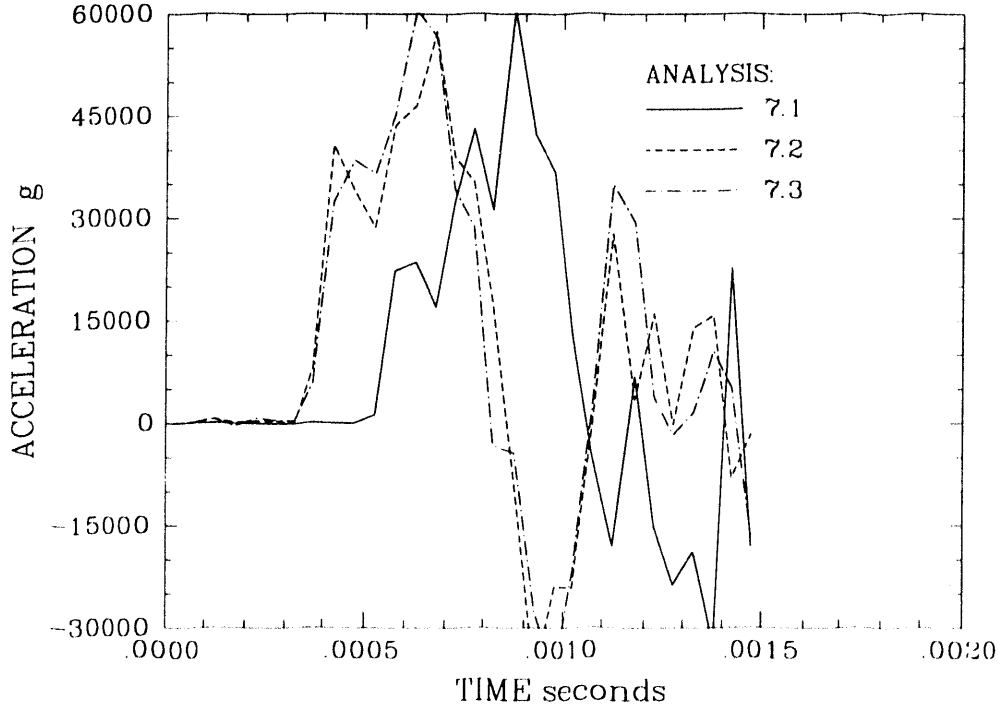

Figure 7.3. Steel Container Acceleration Predicted by the Three-Dimensional Finite Element Analyses of a Side Impact.

Permanent deformations predicted by these analyses are compared with the experimental results in Table 7.2. During the impact experiment, layered material beneath the center of the container was permanently compressed 2.75 inches. The container was deformed 0.082 inches into an oval shape near its midplane (Figure 7.7). Layered material above the container was compressed 2.125 inches. Analysis 7.1 predicted 3.8 inches of layered material crush between the container and the impact surface. Analyses 7.2 and 7.3 both predicted 2.5 inches of layered material crush beneath the container which is reasonably close to the experimental measurement of 2.75 inches. Also, Analyses 7.2 and 7.3 predicted 2.05 inches of layered material crush above the container which is reasonably close to the experimental measurement of 2.125 inches. Thus, reasonable deformation predictions for the wound impact limiter were obtained by using a value of 120 psi for material parameter a.

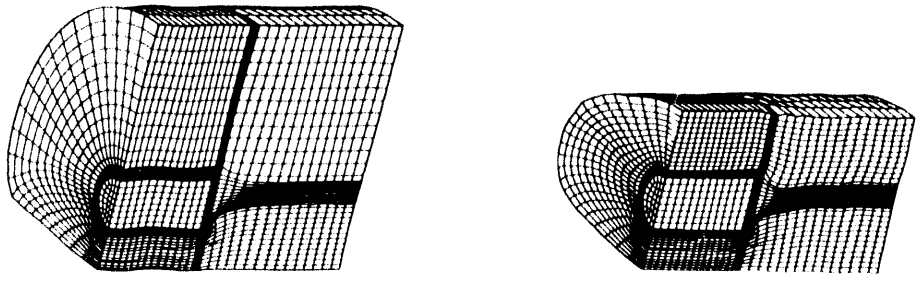

0.8 msec. 1.5 msec.

Figure 7.4. Deformed Shape of the Finite Element Model – Analysis 7.1.

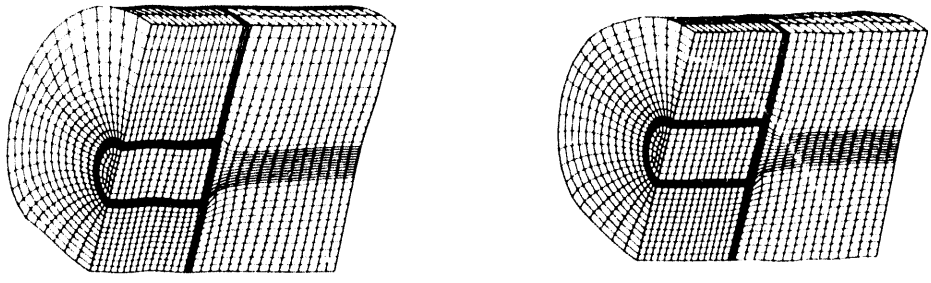

0.8 msec. 1.5 msec.

Figure 7.5. Deformed Shape of the Finite Element Model – Analysis 7.2.

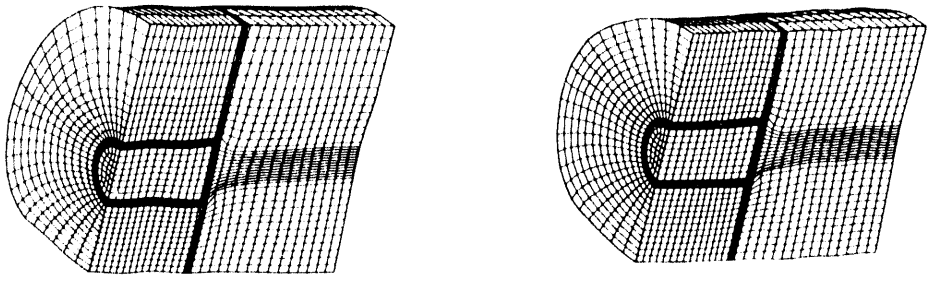

0.8 msec. 1.5 msec.

Figure 7.6. Deformed Shape of the Finite Element Model – Analysis 7.3

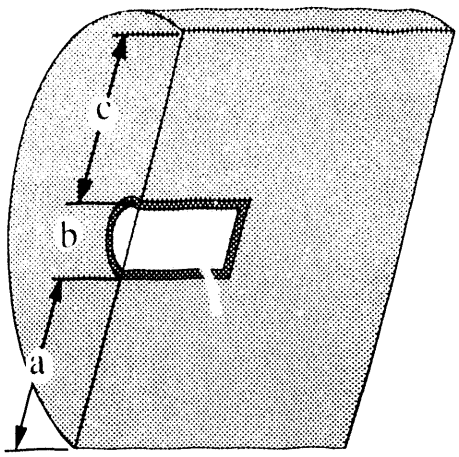

Figure 7.7. Location of Deformation Measurements Summarized in Table 7.2.

Table 7.2. Permanent Deformations Predicted by the Benchmark Analyses

Measurement Location Number	Experimental Measurement (in)	Deformation Predicted by Analysis:		
		7.1 (in)	7.2 (in)	7.3 (in)
a	2.75	3.80	2.50	2.50
b	0.082	0.068	0.080	0.130
c	2.125	3.00	2.05	2.05

Analysis 7.2 predicted that the container would ovalize and be permanently deformed 0.080 inches near its midplane. This prediction is very close to the experimental observation of 0.082 inches. Analysis 7.3 predicted that the steel container would deform 0.130 inches at its midplane. Thus, the container deformation predictions are affected by how the contents are simulated. Predictions for steel container deformation could probably be improved by accurately measuring the stress-strain response of the container material and using, for example, the deviatoric plasticity model with power law hardening which is now available in PRONTO-3D [11]. In these analyses, a simple bilinear stress-strain curve was used to describe the behavior of the steel container.

8. Air Transport Package Analyses - End Impact

A one-fourth scale model of an air transport package was subjected to an end impact with an impact velocity of 650 fps at the rocket sled test facility. In this chapter, results from axisymmetric, two-dimensional analyses of end impact events are presented and compared with the experimental results. These analyses were performed using the axisymmetric finite element model shown in Figure 8.1 and PRONTO-2D [5]. This finite element model represents the package that was subjected to an end impact at the rocket sled test facility. The model includes: the layered material limiter, aluminum load spreader plates, perforated aluminum plugs, the titanium container, and the lead shot contents. The thin stainless steel shell which surrounds the limiter was not included in these analyses because axisymmetric shell elements are not available in PRONTO-2D [5].

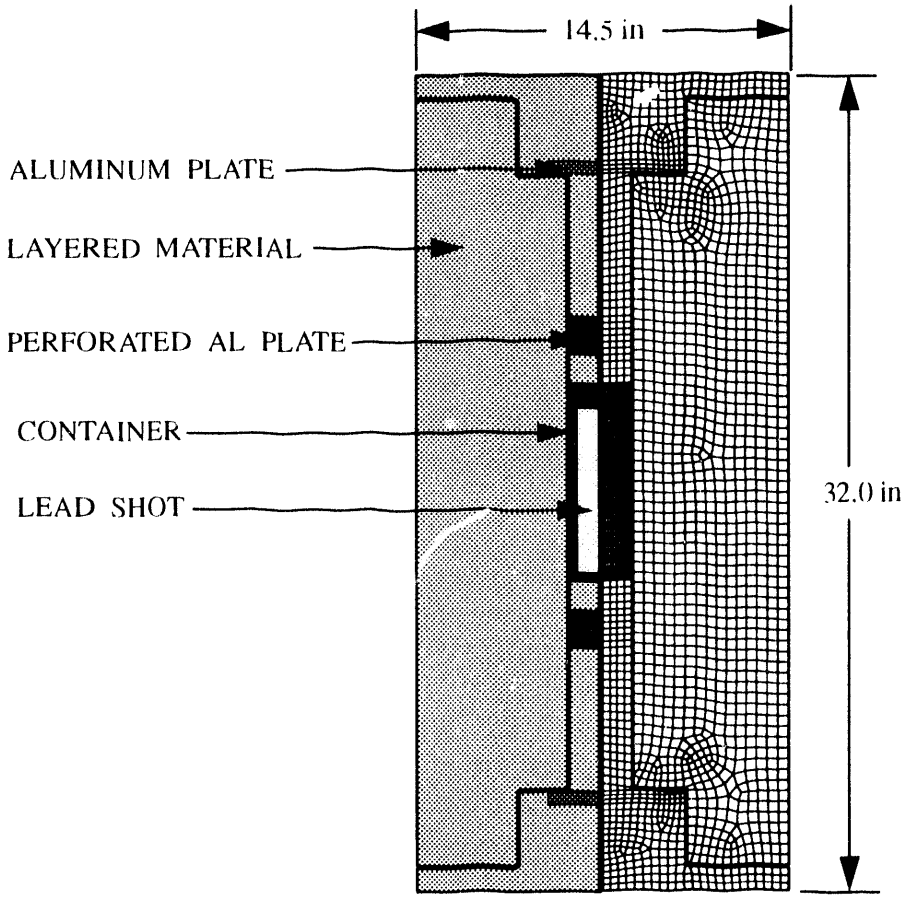

Figure 8.1. Axisymmetric Finite Element Model of an Air Transport Package.

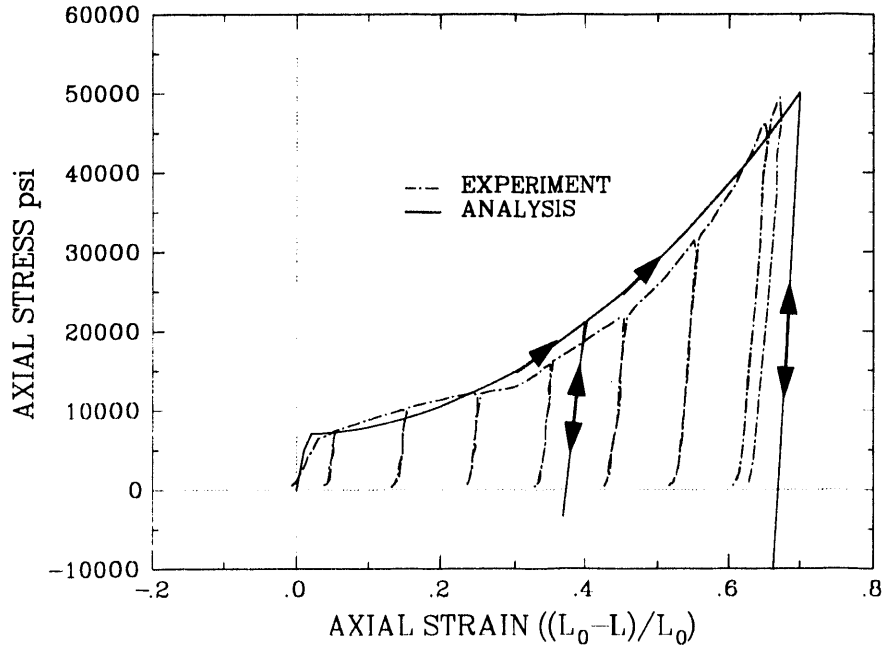

Figure 8.2. Axial Stress-Strain Behavior of Perforated Aluminum Plate Material.

The perforated aluminum plate material was partially characterized with an unconfined compression test. During this test, the perforated aluminum plate behaved much like a rigid foam material (Figure 8.2). The polyurethane foam plasticity model [1] with a yield function given by

$$\Psi^i = -\sigma^i - (a + b\gamma^2) \tag{8.1}$$

was used to simulate the compressive response of this material. To ensure that the modified foam plasticity model captured the behavior of the perforated aluminum plate, the unconfined compression test was analyzed using the finite element model shown in Figure 5.1 and material parameters given in Table 8.1. The analysis revealed that the modified plasticity model would capture the uniaxial response of the perforated aluminum plate (Figure 8.2). The modified plasticity model may not capture the response of the perforated aluminum to other load paths; however, the model is sufficient for the end impact simulation in which the perforated aluminum plate is subjected to uniaxial compression. The behavior of the perforated aluminum material is being thoroughly evaluated by Brown [12].

End impact events were then analyzed using the finite element model shown in Figure 8.1. The material parameters used in these analyses are given in Table 8.1. The material densities were chosen such that the various parts of the model would have the same total mass as the corresponding parts in the actual package. Analyses 8.1 and 8.2 were performed using elastic contents and layered material parameters which are appropriate for precompressed layered material. In the remaining four analyses, the effects of content and layered material modeling variations were investigated. Analyses 8.3 and 8.4 were

Table 8.1. Material Parameters Used in End Impact Analyses

Perforated Aluminum: Modified Plasticity Model						
Analysis Number	Elastic Modulus (psi)	Poisson's Ratio	a (psi)	b		Density (lb s^2 in^{-4})
8.1 to 8.6	5.0×10^5	0.0	7.0×10^3	88.0×10^3		1.3×10^{-4}

Layered Material: New Model						
Analysis Number	Elastic Modulus (psi)	Poisson's Ratio	a (psi)	b	τ (psi)	Density (lb s^2 in^{-4})
8.1, 8.3	1.0×10^5	0.0	120.0	8.68	12,000	3.625×10^{-5}
8.2, 8.4	1.0×10^6	0.0	120.0	8.68	36,000	3.625×10^{-5}
8.5	1.0×10^5	0.0	17.0	8.68	12,000	3.625×10^{-5}
8.6	1.0×10^6	0.0	17.0	8.68	36,000	3.625×10^{-5}

Titanium Container: Elastic-Plastic						
Analysis Number	Elastic Modulus (psi)	Poisson's Ratio	Yield Strength (psi)	Hardening Modulus (psi)	Beta	Density (lb s^2 in^{-4})
8.1 to 8.6	19.0×10^6	0.3	136.0×10^3	15.0×10^3	0.0	4.08×10^{-4}

Lead Shot: Elastic or Elastic-Plastic						
Analysis Number	Elastic Modulus (psi)	Poisson's Ratio	Yield Strength (psi)	Hardening Modulus (psi)	Beta	Density (lb s^2 in^{-4})
8.1, 8.2	40.0×10^3	0.3	-	-	0.0	3.189×10^{-4}
8.3 to 8.6	2.0×10^6	0.3	1200.0	100.0	0.0	3.189×10^{-4}

Aluminum Spreader Plate: Elastic-Plastic						
Analysis Number	Elastic Modulus (psi)	Poisson's Ratio	Yield Strength (psi)	Hardening Modulus (psi)	Beta	Density (lb s^2 in^{-4})
8.1 to 8.6	10.6×10^6	0.3	20.0×10^3	5.0×10^5	0.0	2.60×10^{-4}

Foam Pads: Elastic						
Analysis Number	Elastic Modulus (psi)	Poisson's Ratio	Density lb s^2 in^{-4}			
8.1 to 8.6	1.0×10^5	0.0	3.625×10^{-5}			

identical to Analyses 8.1 and 8.2 except that the contents were modeled as an elastic-plastic material. Analyses 8.5 and 8.6 were identical to Analyses 8.3 and 8.4 except that the layered material parameter a was reduced to 17.0 psi to simulate layered material that is not precompressed. During assembly of the package, the ends of the limiter were manufactured by simply stacking up the layered material inside a stainless steel shell and manually compressing the layers some undefined amount. In Analyses 8.1, 8.3 and 8.5 the package was given an impact velocity of 424 fps and in Analyses 8.2, 8.4 and 8.6 the package was given an impact velocity of 650 fps. In the 650 fps analyses, the layered material was compressed enough such that the layered material obtained a tangent modulus in excess of 1.0×10^5 psi; thus, an elastic modulus of 1.0×10^6 was used for the layered material in these analyses. In the 424 fps analyses, the layered material was given an elastic modulus of 1.0×10^5 psi. This variation in elastic modulus is only expected to affect the predicted rebound velocity of the package. Also, in the 650 fps analyses the tensile strength of the layered material was increased to 36,000 psi so that in the simulations the layered material would remain elastic in tension.

Container displacement and acceleration histories predicted by these analyses are shown in Figures 8.3 and 8.4. The displacement plots show that, as expected, the amount of layered material crush increases with impact velocity. Also, significantly more impact limiter crush is generated in Analyses 8.5 and 8.6 when the layered material is not precompressed. The acceleration plots indicate that the container is subjected to peak accelerations of approximately 30,000 and 60,000 g's during impact events with impact velocities of 424 and 650 fps, respectively. The acceleration plots for Analyses 8.1 and 8.2 indicate that the container will be subjected to acceleration levels in excess of 90,000 g's when the package is rebounding from the impact surface. These high acceleration levels are caused by the elastic contents impacting the inner walls of the container. In Analyses 8.3 to 8.6, the contents were modeled as elastic-plastic materials and high acceleration levels were not generated in the container during rebound.

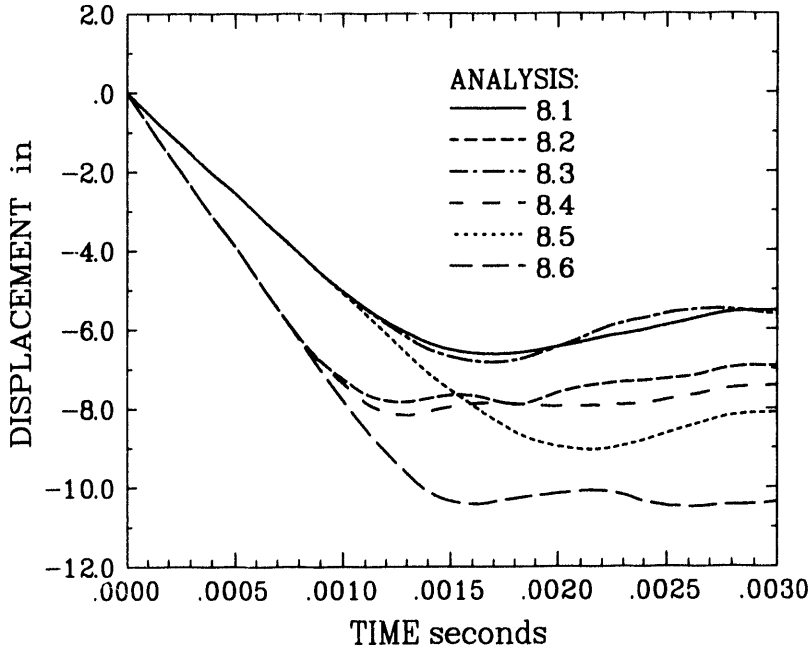

Figure 8.3. Container Displacement Predicted by the End Impact Analyses.

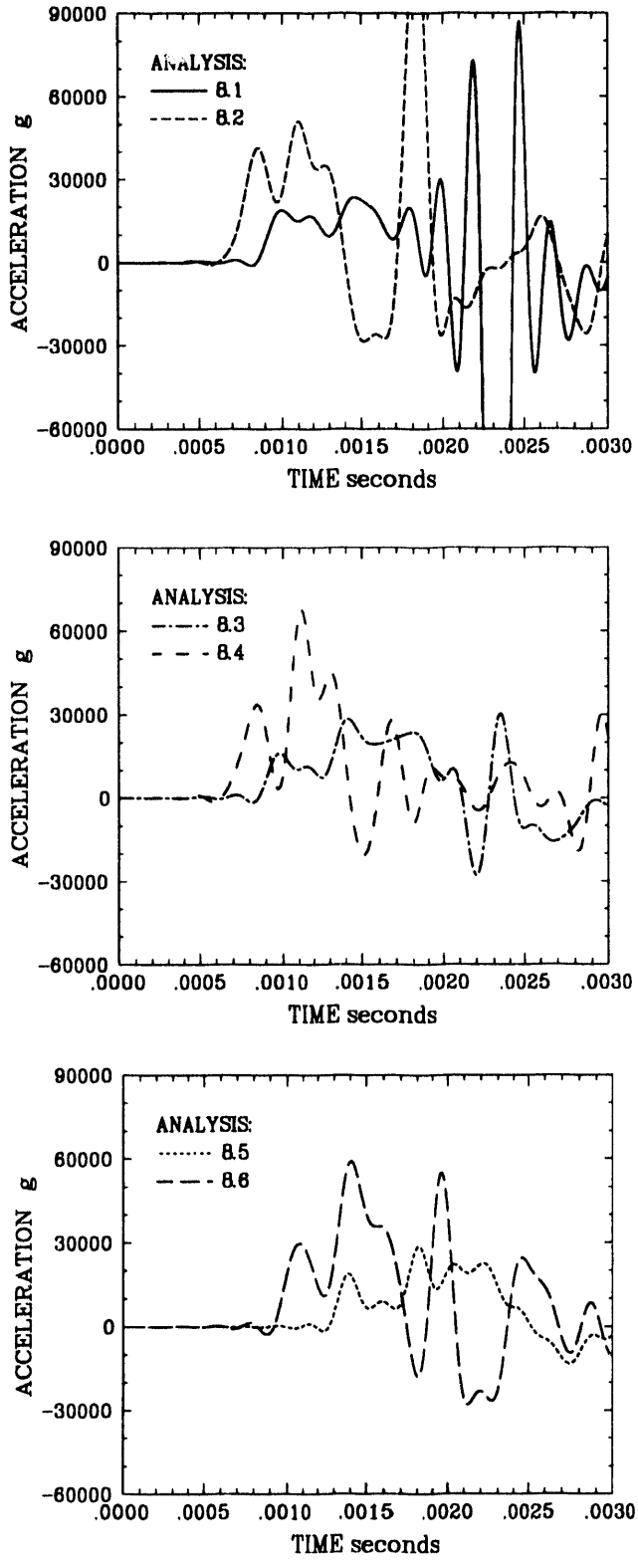

Figure 8.4. Container Acceleration Predicted by the End Impact Analyses.

The end sections of the package limiter have approximately 60 layers of wire mesh and 4 layers of Kevlar fabric per inch. The Kevlar fabric layers alone will give the limiter an initial tensile strength of 5600 psi in directions perpendicular to the axis of the package. Using the procedure outlined in Chapter 7, the predicted maximum tensile load in the Kevlar layers was computed from the maximum principal Cauchy stresses. The predicted maximum tensile load in a single Kevlar layer is given in Table 8.2. Recall that a single Kevlar layer has a tensile strength of 1400 lbs/in. Analyses 8.1, 8.3 and 8.5 indicate that the Kevlar layers will not fail during a 424 fps impact event. Analyses 8.2 and 8.4 predict that Kevlar layers between the aluminum spreader plate and the impact surface will nearly fail during a 650 fps impact event, and Analysis 8.6 predicts failure of these Kevlar layers.

Container and package deformations predicted by these analyses are summarized in Table 8.2. As expected, the impact limiter deforms more when the layered material is not precompressed and when the impact velocity is increased. Plots of the deformed package shape predicted by Analyses 8.2, 8.5 and 8.6 are shown in Figure 8.5. In Analysis 8.2, the contents are elastic and a maximum equivalent plastic strain of 5.3 percent is generated near the end of the container opposite the lid (Figure 8.6). In Analyses 8.4 and 8.6, the contents are elastic-plastic and maximum equivalent plastic strains of 8.9 and 8.1 percent, respectively, are generated near the lid end in the cylindrical wall of the container (Figure 8.6). This plastic deformation leads to bulging of the container and a permanent increase in the outside diameter of the container. Analyses 8.3 and 8.5 indicate that the container will experience little permanent deformation when the impact velocity is reduced to 424 fps.

Table 8.2. Permanent Deformations Predicted by the End Impact Analyses

Analysis Number	Maximum Kevlar Load[1] (lb/in)	Package Height Decrease (in)	Container Height Decrease (in)	Container O.D. Increase (in)
8.1	590	11.0	0.000	0.002
8.2	1360	14.0	0.029	0.006
8.3	640	11.0	0.000	0.001
8.4	1360	14.0	0.120	0.140
8.5	460	16.0	0.000	0.012
8.6	1580	19.2	0.080	0.136
Experiment	-	-	0.120	0.100

[1] Maximum In-plane Tensile Load In a Kevlar Layer.

A scale model package was manufactured and subjected to an end impact at the rocket sled test facility. During this test, a stationary package was impacted with a steel and reinforced concrete block which was carried by a sled and accelerated to a velocity of 650

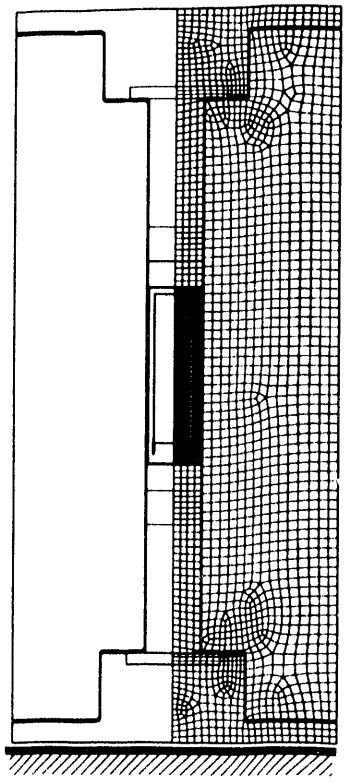

a. undeformed

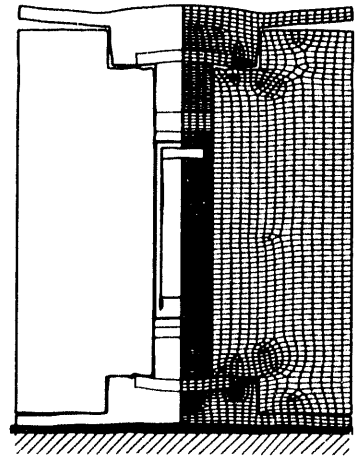

b. Analysis 8.2

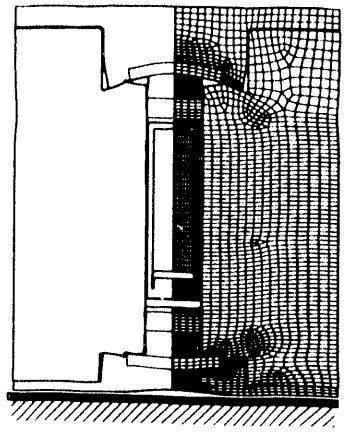

c. Analysis 8.5

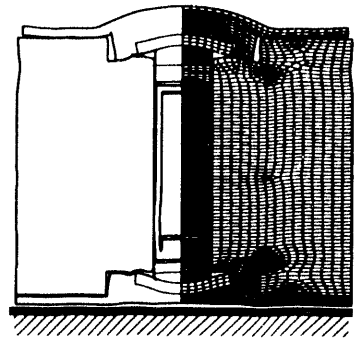

d. Analysis 8.6

Figure 8.5. Deformed Shape of Finite Element Model After End Impact Event.

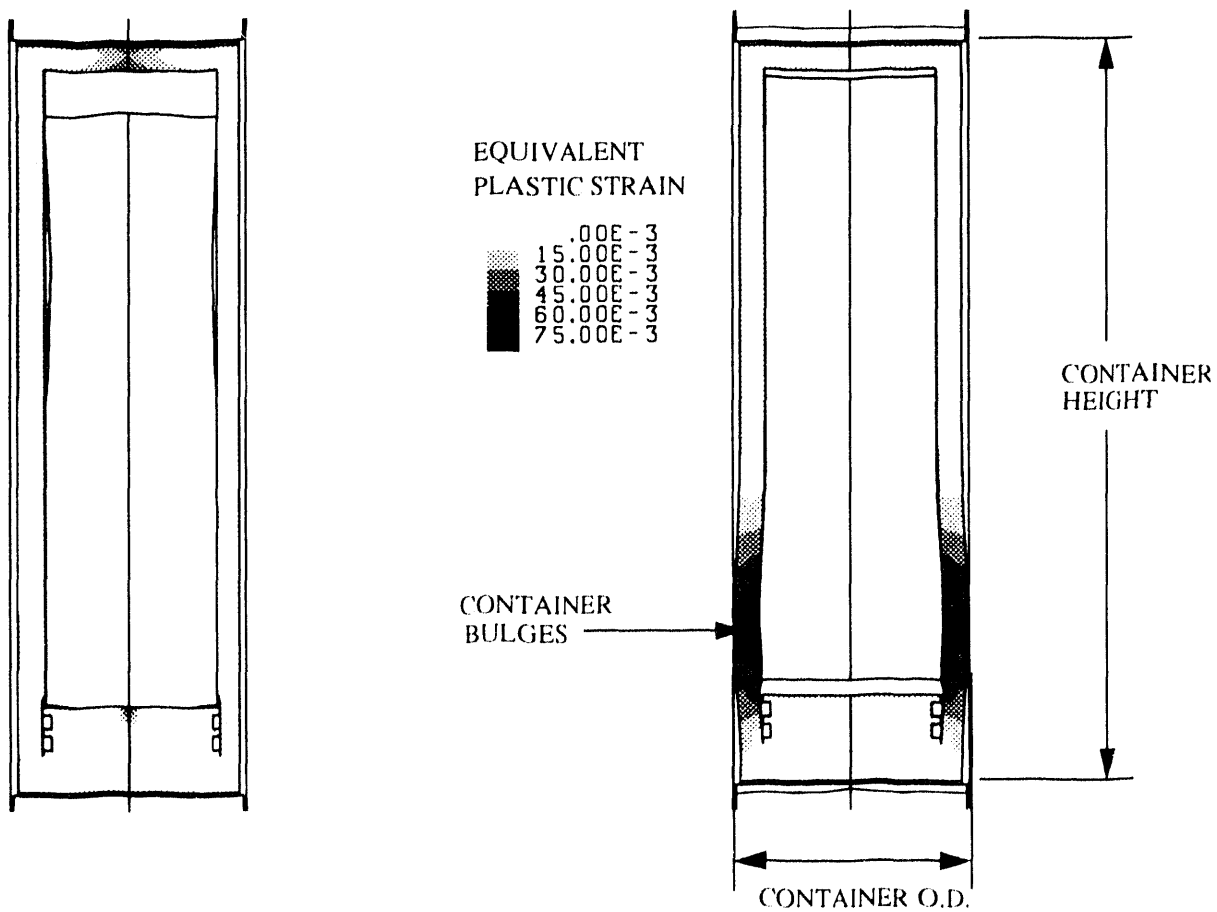

a. Analysis 8.2

b. Analysis 8.6

Figure 8.6. Equivalent Plastic Strain Generated in Container During Impact Event.

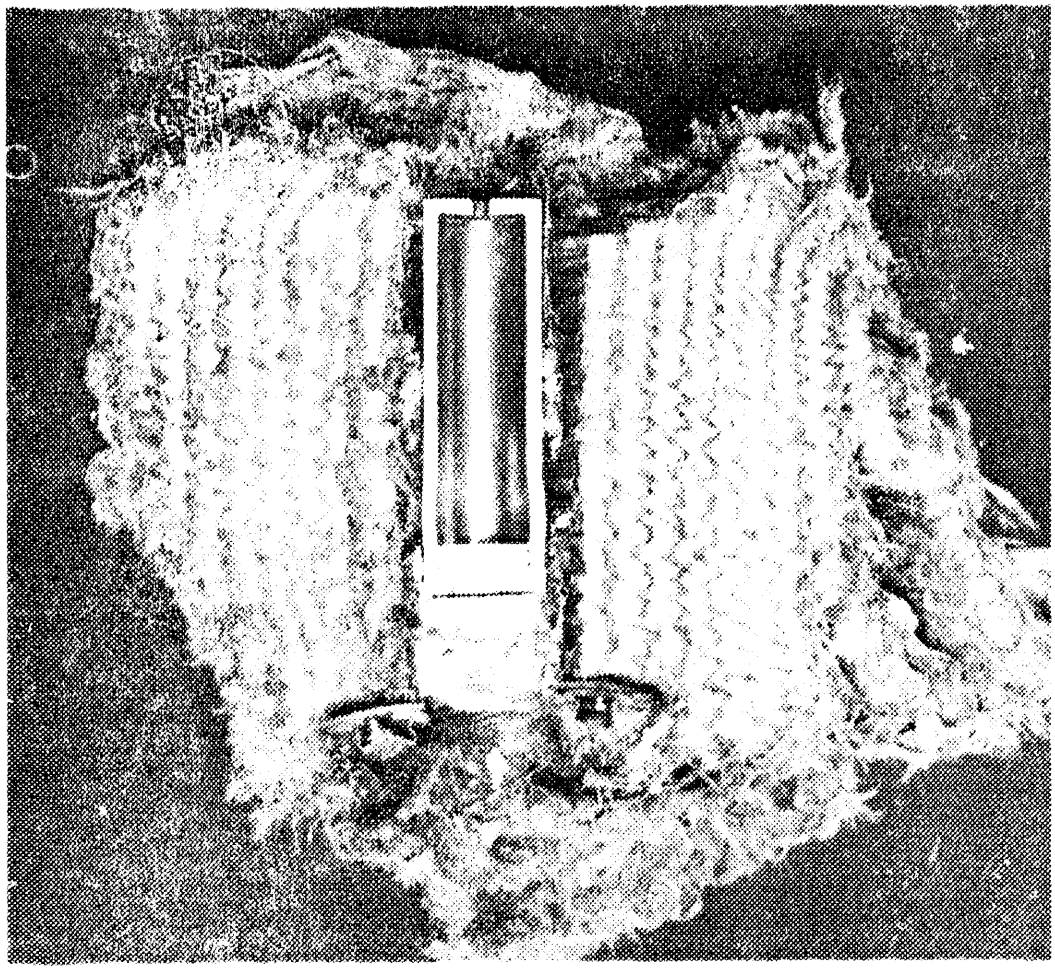

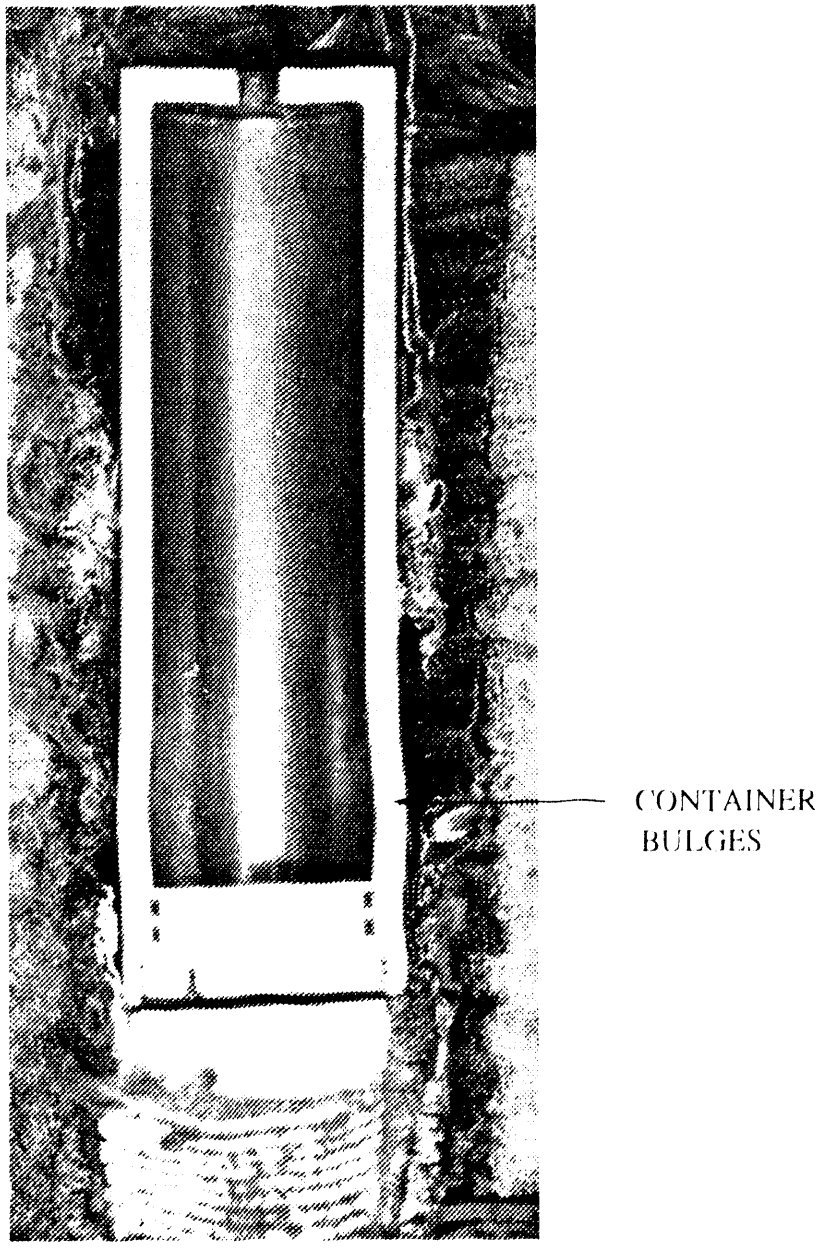

Figure 8.8. Deformed Shape of Sectioned Container After 650 fps End Impact Experiment.

9. Air Transport Package Analyses - Side Impact

A one-fourth scale model of an air transport package with a layered wire mesh and Kevlar fabric impact limiter was subjected to a side impact reverse ballistic test with an impact velocity of 428 feet per second. In this chapter, results from three-dimensional finite element analyses of side impact events are presented and compared with the experimental results. These analyses were performed using the finite element model shown in Figure 9.1 and PRONTO-3D [6]. Only one-half of the package was modeled due to the symmetry present in the package geometry and loading. Appropriate boundary conditions were applied to the symmetry plane. The entire model is shown in the top half of Figure 9.1 and a close-up view of the foam pads, titanium container, and lead contents is shown in the bottom half. The model has a layered material impact limiter which is surrounded by a 304 Stainless Steel shell. The steel shell was modeled using the shell elements in PRONTO-3D [13]. The rest of the package was modeled using three-dimensional continuum elements.

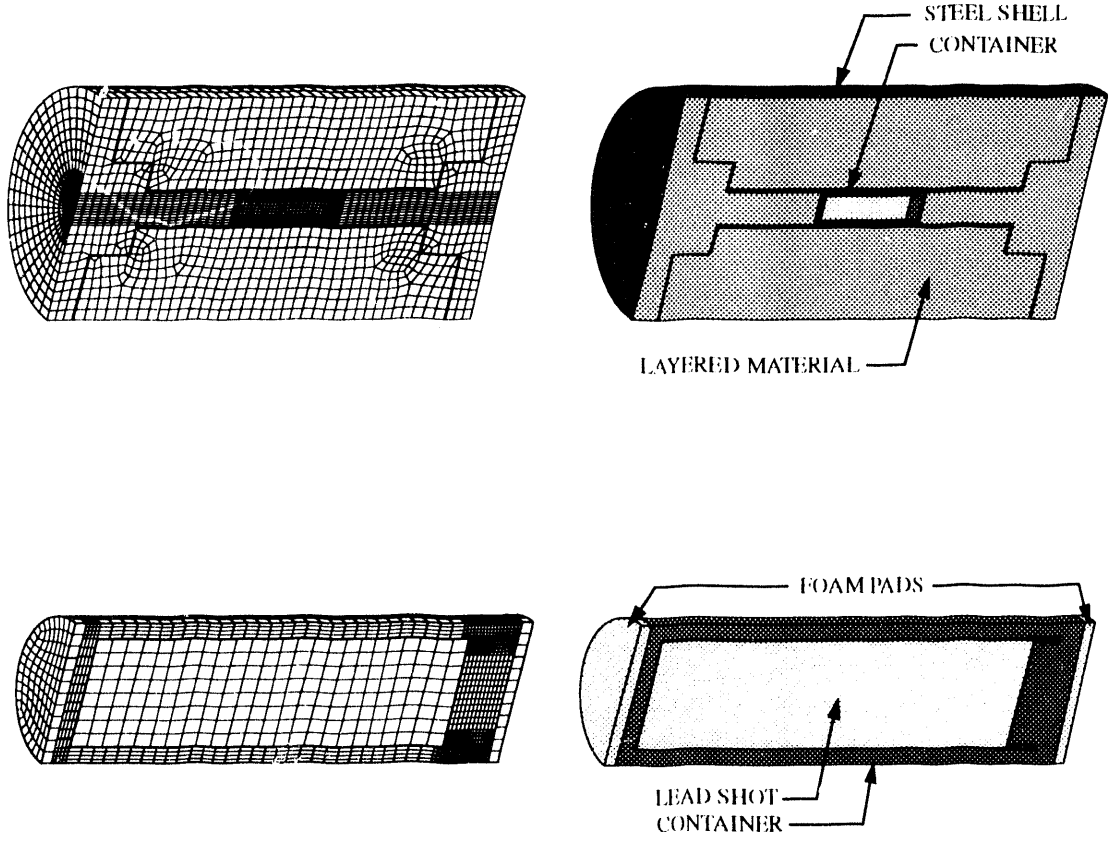

Figure 9.1. Three-Dimensional Finite Element Model of an Air Transport Package.

Table 9.1. Material Parameters Used in the Side Impact Analyses

Layered Material: New Model						
Elastic Modulus (psi)	Poisson's Ratio	a (psi)	b	τ (psi)		Density (lb s^2 in^{-4})
1.0×10^5	0.0	120.0	8.68	12,000		3.625×10^{-5}

Lead Shot: Elastic						
Elastic Modulus (psi)	Poisson's Ratio	Density (lb s^2 in^{-4})				
40.0×10^3	0.3	3.189×10^{-4}				

Titanium Container: Elastic-Plastic						
Elastic Modulus (psi)	Poisson's Ratio	Yield Strength (psi)	Hardening Modulus (psi)	Beta		Density (lb s^2 in^{-4})
19.0×10^6	0.3	136.0×10^3	15.0×10^3	0.0		1.08×10^{-4}

304 Stainless Steel Shell: Elastic-Plastic, Power Law Hardening						
Elastic Modulus (psi)	Poisson's Ratio	Yield Strength (psi)	Hardening Constant	Hardening Exponent	Luder's Strain	Density (lb s^2 in^{-4})
28.0×10^6	0.3	28.0×10^3	192746.0	0.748190	0.0	7.5×10^{-4}

Foam Pads: Elastic						
Elastic Modulus (psi)	Poisson's Ratio	Density (lb s^2 in^{-4})				
1.0×10^5	0.0	3.625×10^{-5}				

Material parameters used in these analyses are given in Table 9.1. The layered material was modeled using the same mechanical parameters as in the previous analysis. The densities of the layered material, titanium container, and lead shot contents were selected such that these components had the same total mass as the actual parts which were used in the side impact experiment. The lead shot was modeled as an elastic material with a low elastic modulus of 40,000 psi. The 304 Stainless Steel shell was modeled using the elastic-plastic, power law hardening material model [11]. The thin foam pads were modeled as an elastic material with the same elastic properties as the layered material.

In the first analysis, the model was subject to an side impact into a rigid target with an impact velocity of 424 fps and in the second analysis the model was given an impact velocity of 650 fps. Displacement and acceleration histories for the container predicted by these analyses are shown in Figures 9.2 and 9.3. The displacement plots indicate that the amount of layered material crush increases with impact velocity. The acceleration plots indicate that the container is subjected to peak accelerations of approximately 55,000 and 85,000 g's for impact velocities of 424 and 650 fps, respectively. The acceleration plots are not very refined since plot data was only stored at time intervals of 0.05 msec.; however, the acceleration history for the 424 fps impact event is similar to the acceleration history shown in Figure 7.3 for the package with a steel container subjected to a 424 fps side impact. These container acceleration levels obtained during side impacts events with the air transport package (Figure 9.3) are significantly higher than the acceleration levels obtained during the end impact events (Figure 8.4).

The cylindrical part of the limiter for this package contained 24 layers of Kevlar fabric and 374 layers of aluminum screen wire. The maximum tensile load in a Kevlar layer was estimated using the procedure outlined in Chapter 7. A comparison of the predicted maximum tensile load with the tensile strength of a single layer, 1400 lbs/in., revealed that the layered material between the container and the impact surface would not fail during a 424 fps impact event but would, at least, begin to fail during a 650 fps impact event. Maximum tensile Kevlar layer loads of 970 lbs/in. and 1930 lbs./in. were predicted for impact velocities of 424 fps and 650 fps, respectively. Additional Kevlar layers should be added to prevent limiter failure during a 650 fps impact event.

A one-fourth scale model package was manufactured and subjected to a side impact at the rocket sled test facility. An impact velocity of 428 fps was generated during this test. As predicted by the finite element analyses, the limiter did not fail in tension during this test. No strain gage or accelerometer data were obtained during the experiment; thus, the only comparisons between analysis and experiment which could be made were of the final deformed shape of the package. Deformed shapes of the models predicted during these analyses are shown in Figures 9.4 and 9.5. The titanium containers stopped moving towards the target at 0.8 msec. and 0.7 msec. during the 424 fps and 650 fps impact events, respectively. The 424 fps and 650 fps analyses were terminated at 1.5 msec. and 1.4 msec., respectively. The deformed shape of a section of the tested impact limiter is shown in Figure 9.6. The predicted deformed shapes of the impact limiters compare reasonably well with the experimental result. However, the analyses indicated that the center of the titanium container would be permanently deformed 0.060 in. during the 424 fps impact event and 0.160 in. during the 650 fps impact event. Measurements of the titanium container after the 428 fps impact indicated that the container was not permanently deformed. This discrepancy could be due to inadequate modeling of the container or the the contents. The two-dimensional analyses of the end impact event which were presented in Chapter 8 showed that the container deformation predictions are significantly affected by content modeling assumptions.

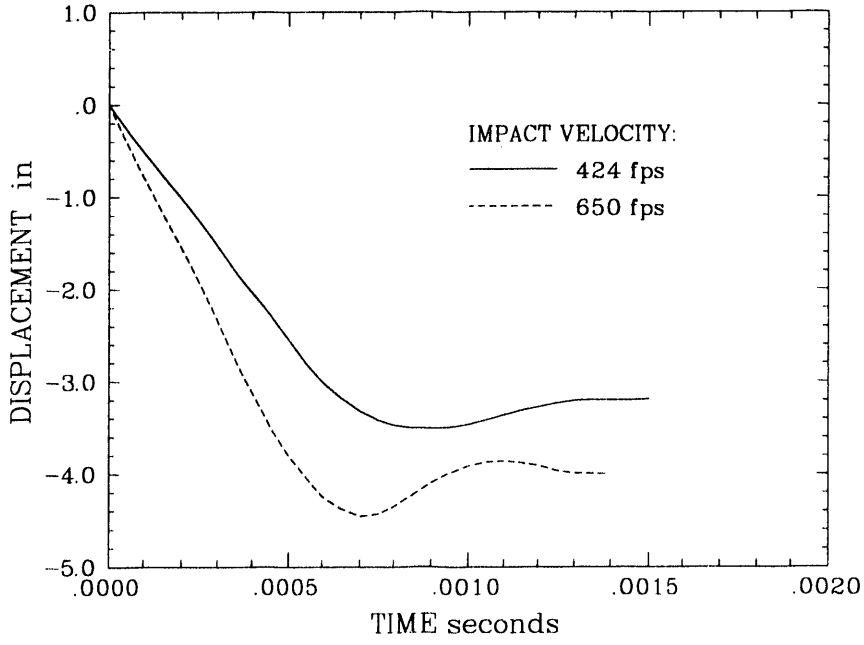

Figure 9.2. Container Displacement Predicted by the Side Impact Analyses.

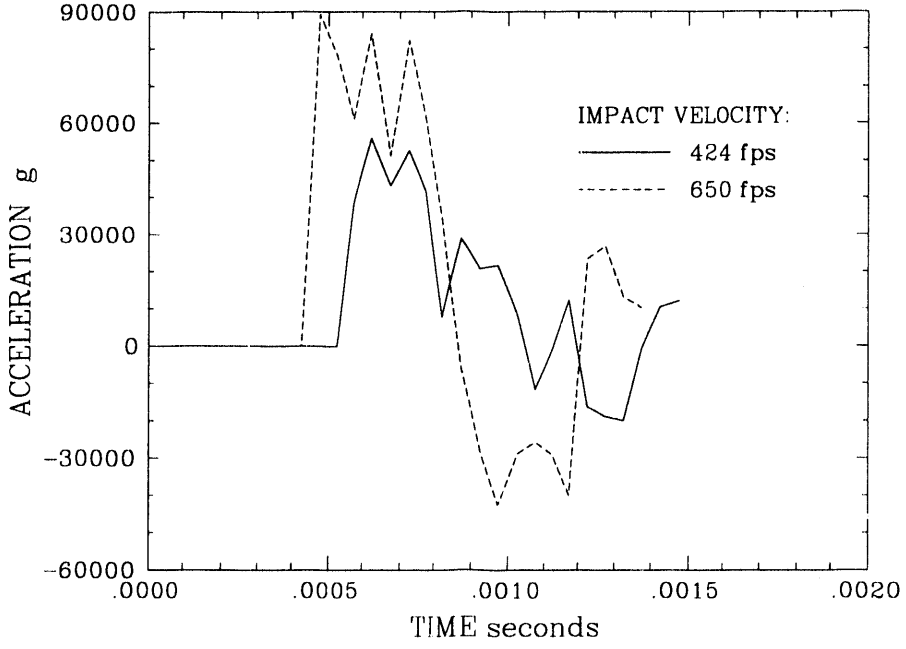

Figure 9.3. Container Acceleration Predicted by the Side Impact Analyses.

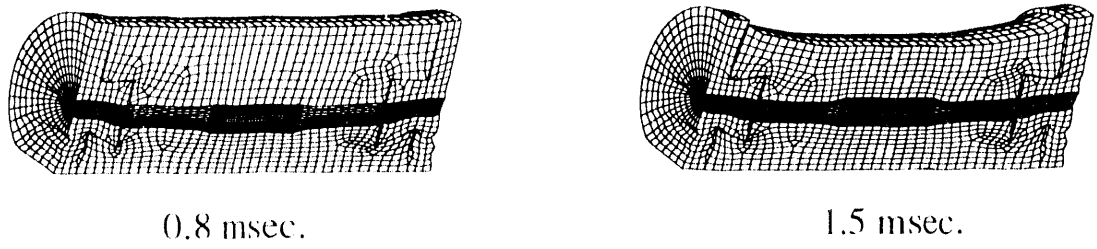

Figure 9.4. Deformed Shape of Finite Element Model - 424 fps Side Impact.

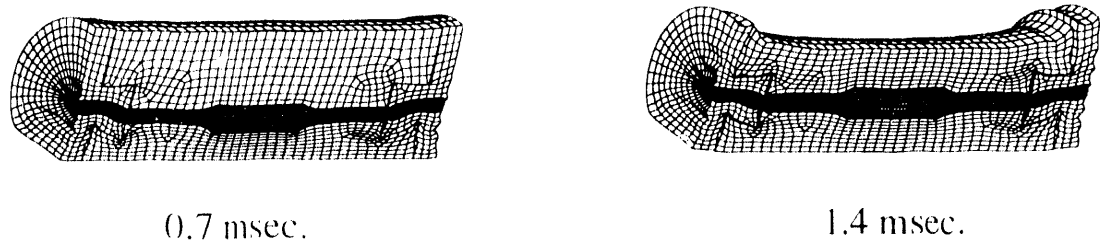

Figure 9.5. Deformed Shape of Finite Element Model - 650 fps Side Impact.

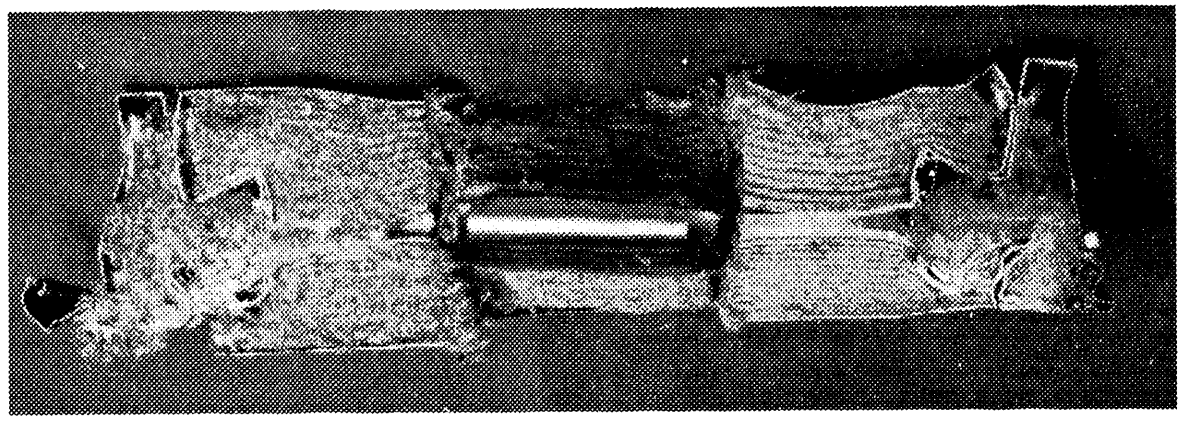

Figure 9.6. Deformed Shape of the Impact Limiter After it was Sectioned - 428 fps Side Impact Experiment.

10. Summary

An isotropic plasticity model for composite layered wire mesh and Kevlar fabric material has been developed and used in the investigation of hypothetical air transport package accidents. Results from a limited number of unconfined and confined compression tests were used to obtain material parameters for the new layered material model. The material characterization experiments were then analyzed to ensure that the new plasticity model captured the material behavior exhibited during these tests. The new plasticity model accurately captures the isotropic compressive response of the layered material but does not capture: (1) increases in the elastic stiffness as the material is compressed and (2) anisotropic tensile response and layer separation. A material model which captures the increase in layered material stiffness as it is compressed was recently developed by Krieg and Brown [3, 12]. This new model should be used in future analyses of hypothetical accidental impact events. The current investigation revealed that an accurate simulation of the anisotropic tensile response of the layered material is not needed to generate accurate load transfer and container deformation predictions; thus, an isotropic model for the layered material should be adequate for most impact event simulations.

Results from both the finite element analyses and the experiments indicate that a composite layered wire mesh and Kevlar fabric impact limiter will remain intact during a 650 fps impact event if the number of Kevlar layers is adequate. However, the layered wire mesh and Kevlar fabric impact limiter allows for the transmission of rather high load levels to the primary inner container. The primary container was not plastically deformed during the 428 fps side impact experiment but was plastically deformed during the 650 fps end impact experiment. The amount of load transmitted to the primary container may be reduced by either adding wire mesh layers or replacing the wire mesh layers with layers of material which absorb more energy than the wire mesh. These modifications to the baseline design should be investigated further. Also, the analyses presented in this report reveal that content behavior can have a significant positive or negative effect on primary container deformation. For example, the 650 fps end impact simulation revealed that the internal pressure generated by the plastically deforming contents contributes to the undesirable bulging of the containment vessel. Content behavior must be considered in the development of air transport package designs.

11. References

1. M.K. Neilsen, H.S. Morgan, and R.D. Krieg, *A Phenomenological Constitutive Model for Low Density Polyurethane Foams*, SAND86-2927, Sandia National Laboratories, Albuquerque, NM, April 1987.

2. S.W. Attaway, *A Local Isotropic / Global Orthotropic Finite Element Technique for Modeling the Crush of Wood* , SAND88-1449, Sandia National Laboratories, Albuquerque, NM, 1988.

3. R.D. Krieg and K. Brown, *Computer Modeling of Wrapped Impact Limiters*, Final Report 98-816, University of Tennessee, Knoxville, TN, September 1992.

4. C.M. Stone, *SANTOS A Two-Dimensional Finite Element Program for the Quasistatic, Large Deformation, Inelastic Response of Solids*, SAND90-0543, Sandia National Laboratories, Albuquerque, NM, in preparation

5. L.M. Taylor and D.P. Flanagan, *PRONTO-2D A Two-Dimensional Transient Solid Dynamics Program*, SAND86-0594, Sandia National Laboratories, Albuquerque, NM, March 1987.

6. L.M. Taylor and D.P. Flanagan, *PRONTO-3D A Three-Dimensional Transient Solid Dynamics Program*, SAND87-1912, Sandia National Laboratories, Albuquerque, NM, March 1989.

7. Krieg, R.D., *A Simple Constitutive Description for Soils and Crushable Foams*, SC-DR-72-0883, Sandia National Laboratories, Albuquerque, NM, 1978.

8. Reuter, R.C. and Allen, J.J., *Prediction of Mechanical States in Wound Capacitors*, ASME Journal of Mechanical Design, Vol. 113, December 1991.

9. Van Vlack, L.H., **Materials Science for Engineers**, Addison Wesley, Reading, MA, 1970.

10. Rack, H.J., and Knorovsky, G.A., *An Assessment of Stress-Strain Data Suitable for Finite-Element Elastic-Plastic Analysis of Shipping Containers*, SAND77-1872, Sandia National Laboratories, Albuquerque, NM, September 1978.

11. C.M. Stone, G.W. Wellman, and R.D. Krieg, *A Vectorized Elastic Plastic Power Law Hardening Material Model Including Luders Strain*, SAND90-0153, Sandia National Laboratories, Albuquerque, NM, March 1990.

12. K.H. Brown, *A Large Volume Strain Plasticity Constitutive Model for Impact Limiter Materials*, M.S. Thesis, Engineering Science and Mechanics Department, The University of Tennessee, Knoxville, TN, December 1992.

13. V.L. Bergmann, *Transient Dynamic Analysis of Plates and Shells with PRONTO-3D*, SAND91-1182, Sandia National Laboratories, Albuquerque, NM, September 1991.

Unlimited Release

U. S. Department of Energy
Office of Civilian Waste Management
Attn: W. Lake, RW-431
Mail Stop RW-40
1000 Independence SW
Washington, DC 20585

U.S. Department of Energy
Northwestern On-Site
Remediation Branch
Attn: J. C. Lehr, EM-442
Mail Stop EM-442
B-205
19901 Germantown Road
Germantown, MD 20585

U.S. Department of Energy
Office of Waste Operations
Attn: S. P. Cowen, EM-30
Mail Stop EM-30
A-214A
19901 Germantown Road
Germantown, MD 20585

U.S. Department of Energy (2)
Office of Waste Operations
Attn: J. Lytle, EM-30
L. Harmon, EM-30
Mail Stop EM-30
7A-049
1000 Independence SW
Washington, DC 20585

U.S. Department of Energy (5)
Attn: L. Blalock, EM-561
R. Brancato, EM-561
M. Conroy, EM-561
M. Keane, EM-561
E. McNeil, EM-561
Mail Stop EM-561
Washington, DC 20585-0002

U.S. Department of Energy
Oak Ridge Operations Office
Attn: M. Heiskell
P.O. Box E
Oak Ridge, TN 37831

U.S. Department of Energy (4)
Albuquerque Operations Office
Albuquerque Headquarters
Attn: J. Bickel
K. G. Golliher
P. A. Saxman
D. Bandy
P.O. Box 5400
Albuquerque, NM 87115

Argonne National Laboratory
Attn: G. Popper
9700 South Cass Ave.
Argonne, IL 60439

U.S. Department of Transportation
Office of Materials Transportation
Attn: K. Smith
400 Seventh Street, SW
Washington, DC 20590

U.S. Nuclear Regulatory Commission (2)
Office of Nuclear Materials Safety
and Safeguards
Attn: R. Chappell
C. MacDonald
Washington, DC 20555

Gus Aramayo
Oak Ridge National Laboratory
P.O. Box 2008
MS-6332
Oak Ridge, TN 37831

Ermes DeMaria
Senior Transportation Safety Specialist
Radiopharmaceutical Division
Du Pont Merck Pharmaceutical Company
331 Treble Cove Road
North Billerica, MA 01862

Frank Falci
8905 Copenhaver Drive
Potomac, MD 20854

Paul Hagan
U.S. Department of Energy/Rocky Flats
P.O. Box 928
Golden, CO 80401

James Hummer
Westinghouse - Hanford Co.
P.O. Box 1970
MS G2-02
Richland, WA 99352

Prof. Ray Krieg (5)
Engineering Science and Mechanics
301 Perkins Hall
University of Tennessee
Knoxville, TN 37923-6819

Eric Opperman
Packaging and Transportation Group
Westinghouse Savannah River Company
Savannah River Laboratories
P.O. Box A
Aiken, SC 29802

Joanne Passaglia
Transportation Management Program
Office of Technology Development
U.S. Department of Energy
Trevion II Building, EM-561
Washington, DC 20585

Bill Pearson
U.S. Department of Energy
704 S Area
Field Office, Savannah River
P.O. Box A
Aiken, SC 29808

Ronald Pope
Oak Ridge National Laboratory
P.O. Box 2008
Building 4500N, MS-273
Oak Ridge, TN 37831-6273

Frank Punch
Packaging and Transportation Specialist
EH-33.3 GTN
U.S. Department of Energy
Washington, DC 20585-0001

Prof. H.L. Schreyer
Dept of Mechanical Engineering
University of New Mexico
Albuquerque, NM 87131

James Szenasi
OPEP
U.S. Department of Energy
Field Office, Albuquerque
P.O. Box 5400
Albuquerque, NM 87115

Bob Towell
U.S. Department of Energy
19901 Germantown Road, EH-33.3
Germantown, MD 20874

Mike Wangler
Transportation and Packaging
Safety Division
U.S. Department of Energy, EH-33.3
Room 6138
19901 Germantown Road
Germantown, MD 20874

Internal Distribution:

0324 P.E. D'Antonio
0333 C.G. Shirley
1425 J.H. Biffle
1425 S.W. Attaway
1425 M.L. Blanford
1434 D.R. Martinez
1500 D.J. McCloskey
1501 C.W. Peterson
Route to: 1512, 1513, 1551, 1552
1502 P.J. Hommert
Route to: 1503, 1511, 1553, 1554
1561 H.S. Morgan
1561 M.K. Neilsen (15)
1561 M.W. Heinstein
1561 E.L. Hoffman
1561 C.M. Stone
1561 J.R. Weatherby
1561 G.W. Wellman
1562 R.K. Thomas
1562 F.J. Mello
1562 G.D. Sjaardema
5165 N.R. Hansen
5365 G.C. Story
5365 R.D. Monson
6000 D.L. Hartley
6600 J.B. Woodard
6603 R.E. Luna
Attn: TTC Master File
6603 TTC Library (15)
6641 R.P. Sandoval
6641 J.D. McClure
6642 G.F. Hohnstreiter
6642 D.J. Ammerman
6642 J.G. Bobbe
6642 D.L. Bolton
6642 D.C. Harding
6642 J.D. Pierce (15)
6642 K.B. Sorenson
6642 H.R. Yoshimura
6643 T.L. Sanders
8246 W.Y. Lu
8401 C.L. Knapp
8702 C.W. Robinson
8741 G.A. Benedetti
8741 M.L. Chiesa
8742 P.E. Nielan
8743 M.L. Callabresi
8746 W.A. Kawahara
7141 Technical Library (5)
7151 Technical Publications

7613-2 Document Processing for DOE/OSTI (10)
8523-2 Central Technical Files

DATE
FILMED
1/3/94
END